

Basic Physics of Radionuclide Imaging

CRAIG LEVIN

Molecular Imaging Program, Stanford University School of Medicine, Stanford, California

- I. Where Do the Nuclear Emissions Used in Radionuclide Imaging Come From?
- II. Relevant Modes of Nuclear Decay for Medical Radionuclide Imaging
- III. Production of Radionuclides for Imaging
- IV. Interactions of Nuclear Emissions in Matter
- V. Exploiting Radiation Interactions in Matter for Emission Imaging
- VI. Physical Factors That Determine the Fundamental Spatial Resolution Limit in Nuclear Imaging

Radioisotope imaging is the *in vivo* imaging of physiological function using radiation emanating from radionuclides in tracer quantity inside the subject. Physics is involved in almost every step, from the production and decay of the radionuclide to the formation and analysis of the resulting images. In this chapter we discuss some basic physics topics that are relevant to imaging of nuclear emissions. More in-depth discussions can be found in the references given at the end of this chapter, especially in Rollo (1977) and Sorenson and Phelps (1987). Because later chapters deal with the topics of radiation detectors (Part IV) and imaging systems (Parts II, III, and V) used in nuclear emission imaging, we do not cover the topics of radiation detector and imaging system instrumentation physics in full detail in this chapter.

I. WHERE DO THE NUCLEAR EMISSIONS USED IN IMAGING COME FROM?

A. Nuclear Constituents

The atomic nucleus consists of neutrons and protons, also known as *nucleons*. The proton has one unit of fundamental electronic charge, whereas the neutron is electrically neutral. The size and shape of the nucleus depends on the number of neutrons (N) and protons (Z), their particular energy states, and the angular momentum of the nucleus. A typical nuclear diameter is on the order of 10^{-12} – 10^{-13} cm and the density of nuclear matter is roughly 10^{14} g/cm³. The total number of nucleons in a nucleus (A) is known as the *mass number*. A *nuclide* has a particular nuclear composition with mass number A , *atomic number* Z and *neutron number* N . The notation we use to identify a particular nuclear composition of an atomic element E with atomic number $A = Z + N$ is ${}^A_Z E$, ${}_Z E^A$, or just ${}^A E$. Atomic species with identical chemical properties (same Z) but distinct masses (different A) are called *isotopes*. Nuclides with the same A are called *isobars*; those with the same N are called *isotones*. Because chemical reactions involve primarily the outermost orbital electrons of the atom, in general, labeling a compound with a radioactive isotope will not change its chemical behavior. Likewise, the chemical state of an atom

does not affect its nuclear radioactive characteristics. These are key concepts to the development of radiotracers for nuclear medicine that are discussed in the next chapter.

B. Nuclear Forces and Binding Energy

Three out of the four fundamental interactions in nature play important roles within the nucleus. The *electromagnetic* interaction is responsible for repulsive Coulomb forces among the protons within a nucleus (because the neutron is electrically neutral, it does not interact electrically). Because a typical distance between protons in a nucleus is $\sim 10^{-11}$ cm, these electrostatic repulsion forces are immense. The *strong* nuclear interaction is an attractive force occurring between nucleons within the nucleus irrespective of their electronic charge and is responsible for holding together the nucleus in the face of the large electrostatic repulsion between protons. This interaction's name comes from the fact that it is typically over a factor of 100 times stronger than the electromagnetic interaction between protons within the nucleus. The *weak* nuclear force is responsible for certain types of radioactive decay of which spontaneous nuclear β decay is an example. The weak interaction is typically a factor of 10^{-3} – 10^{-4} weaker than the electromagnetic interaction. In current theories of elementary particles, the weak and electromagnetic forces are considered different manifestations of the same fundamental electro-weak interaction. The fourth fundamental force of nature, gravity, has negligible effects within the nucleus because the gravitational forces between the relatively light nucleons ($\sim 10^{-27}$ kg) are roughly a factor of 10^{-36} weaker than the typical electromagnetic forces between them.

The *binding energy* is the energy (in the form of work) required to overcome the forces holding an atomic species together and separate it into its individual, unbound constituents: neutrons, protons, and orbital electrons. Basically, if you add up the masses of these individual components, the sum is greater than the mass of the combined nucleus, and the difference is the binding energy. Conversely, the binding energy is the energy that would be released if the separated constituents were assembled into a nucleus. The energy required just to strip the orbital electrons from the atom is negligible compared to that portion of the binding energy required to separate the nucleons, called the *nuclear binding energy*. From Einstein's mass–energy equivalence equation, $E = mc^2$, we can therefore write the binding energy $B_{\text{tot}}(A, Z)$ as:

$$B_{\text{tot}}(A, Z) = [ZM_H + NM_n - M(A, Z)]c^2 \quad (1)$$

where M_H and M_n are the masses of the hydrogen atom and neutron, respectively, and we have written the expression in terms of atomic rather than nuclear mass for convenience.

C. Nuclear Energy Levels

The motions of nucleons under the influence of the fundamental forces within the nucleus are quite complex. One of the most successful models describing the energy states of nucleons within a nucleus is the *shell model*. In this model, nucleons move in orbits about one another in analogy to Bohr's atomic shell model, which describes the motion of orbital electrons about the nucleus. The types of motions allowed are *quantized*, that is, described by discrete nuclear quantum number parameters. The result is a unique set of allowed discrete energy states, called *energy levels*, for each of the nucleons in a nucleus. The most stable arrangement of nucleons in which the entire system has the lowest overall energy is called the ground state. Excited states of the nucleus, in which the nucleons occupy elevated energy states, exist typically for extremely short times before transforming or *decaying* to a different lower energy state. Those excited states of an atomic species E that are maintained for a relatively long period of time (≥ 1 ns) before decay are called *metastable* states and denoted by mE . If one nuclide is a metastable state of another, they are termed *isomers*. An example of a metastable state is ^{99m}Tc , which is currently the most commonly used gamma-ray emitter in nuclear medicine imaging. Changes in nucleon configurations are nuclear transitions between the discrete nuclear energy states or levels in analogy to rearrangements of orbital electrons in the atomic shell structure.

Figure 1 shows a simplified version of the nuclear *energy level diagram* relevant to the generation and decay of ^{99m}Tc . A typical level diagram shows the ground and excited energy states of the nucleus (depicted as horizontal lines with corresponding radiation energies) as well as the allowed transitions between higher and lower energy levels (vertical arrows with relative transition probabilities listed).

D. Nuclear De-excitation

A fundamental property in nature is that systems tend to evolve from higher to lower energy states. Nuclear transitions from higher to lower states of the same nuclide are electromagnetic in nature and result in the emission of electromagnetic radiation. The electric and magnetic fields are created for a very short time as one or more nucleons in the nucleus rearrange themselves during a transition from an initial to a final state. The energy available from this reconfiguration can be released in two ways. The first is in the form of *gamma-ray* photons. Gamma rays are the most commonly used nuclear emissions in radioisotope imaging. The second transition process by which an excited nucleus can relax is known as *internal conversion*. In this process, the nuclear energy is transferred directly to an atomic electron (usually inner shell). These transitions are somewhat analogous to that which occurs in inner shell

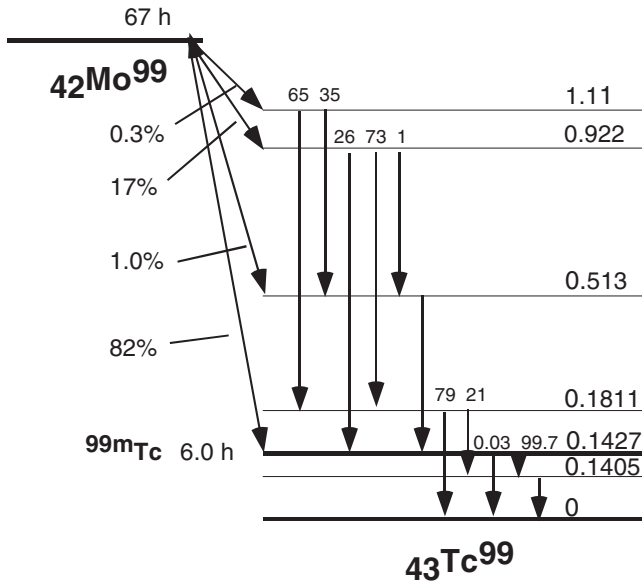


FIGURE 1 Relevant nuclear energy level diagram of the ^{99}Mo - ^{99}Tc system for the generation and decay of $^{99\text{m}}\text{Tc}$. Level energies shown are in MeV. The 6.0-hour half-life decay of $^{99\text{m}}\text{Tc}$ results in a two-photon cascade of 2.2 and 140.5 keV gamma rays. The 2.2 keV photon is absorbed before reaching the detector in most imaging applications. (Adapted from Lederer *et al.*, 1967.)

atomic transitions in high- Z materials. When excited electrons in an inner shell of a high- Z atom transition from higher to lower energy levels, electromagnetic emission of a *characteristic X-ray* or ejection of an *Auger electron* occurs to carry away the available excitation energy. (Note that Auger electrons, however, are more likely released from outer atomic shells.) Thus, the competition between gamma-ray and internal-conversion electron emission in nuclear transitions is somewhat analogous to the alternate emission of an X-ray or Auger electron as a result of atomic transitions involving inner-shell electrons of a high- Z atom. Internal-conversion electrons are rapidly absorbed in tissue and are thus not directly useful in radioisotope imaging.

When energy is released in a nuclear transition from a higher to lower energy state, from say a gamma-ray emission, the binding energy of the nucleus increases and the mass decreases. Thus, some of the available nuclear mass is converted into energy. The energy released is called the *transition energy*. Usually, the larger the energy difference between initial and final states, the greater the transition rate. Differences in nuclear *spin* and *parity* of the two states involved also play a crucial role in determining the transition rate, in analogy to atomic transitions. For transitions to occur from lower to higher energy states, external energy must be furnished, as is the case in *nuclear reactions*. This topic is discussed in a subsequent section when we discuss radioisotope production.

E. Nuclear Stability

There is a tendency toward instability especially in systems comprising a large number of identical particles confined in a small volume. An unstable nucleus emits photons and/or particles in order to transform itself into a more stable nucleus. This is what is meant by *radioactive decay*, and nuclides undergoing such transformations are called *radionuclides*. Studies of radioactivity are the basis for our understanding of the atomic nucleus. The process of nuclide formation favors nuclides with higher binding energy. Larger binding energy and lower mass mean more-stable nuclei. However, the more nucleons, the greater the total binding energy. Thus, a more-appropriate measure of stability is the average *binding energy per nucleon*, B_{tot}/A . Higher B_{tot}/A values indicate greater stability. For nuclides with mass number $A > 20$, B_{tot}/A lies between 8 and 9 MeV per nucleon, with a maximum at $A \approx 60$ and a slow decrease for higher values of A .

There are certain nucleon configurations that result in more-stable nuclei, and there are a few key factors contributing to this stability. Figure 2 shows schematic plots of neutron number N versus atomic number Z for experimentally determined stable (higher binding energy, lower mass) odd- A and even- A nuclei. The different line thickness for odd- and even- A plots represents the fact that there are more stable isotopes and isotones for even- A nuclei. For light nuclides, the average *line of stability* clusters around $N \approx Z$ (equal number of protons and neutrons); for heavier ones, it deviates from this ($N \approx 1.5Z$) because of the increasing contribution of the Coulomb repulsive force toward instability for higher Z . An excess of neutrons and

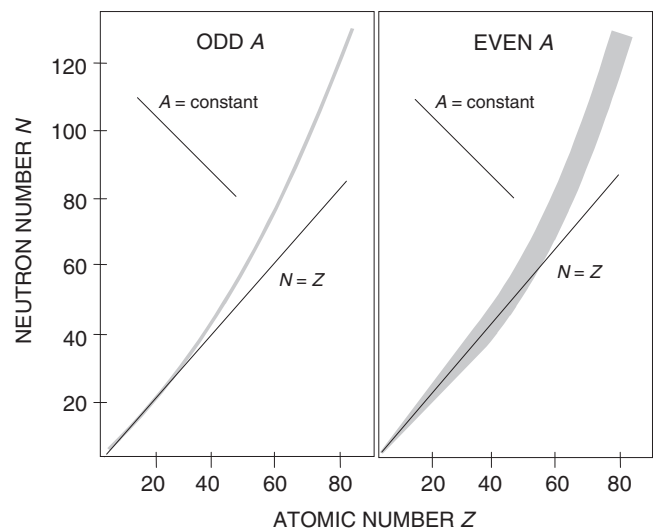


FIGURE 2 Depiction of neutron number versus proton number for stable odd- A (left) and even- A (right) nuclides. (Adapted from Meyerhof, 1967.)

the accompanying strong nuclear force is required in heavy nuclei to overcome the long-range Coulomb repulsive forces between a large number of protons.

For odd A , usually only one stable isobar exists. For even A , usually only even N –even Z nuclides exist. Even–even nuclides occur most frequently. Of the 281 known stable nuclides, 165 of them are even N –even Z , 53 are even N –odd Z , 57 are odd N –even Z , and only 6 are odd N –odd Z . Particularly high stability (higher binding energy) and high abundance with respect to neighboring species are seen for nuclides with N or Z equal to 2, 8, 20, 28, 50, 82, and 126, called the *magic numbers*. In the shell model it is supposed that the magic numbers reflect effects in nuclei very similar to the closing of electronic shells in atoms. The additional stability associated with even nucleon number (even N or Z or both) reflects the tendency of nuclear stability through the *pairing up* of identical nucleons (with opposite spins), similar to electrons in atomic orbitals. The further a nuclide is from the line of stability, the more likely it is to be unstable. All nuclides heavier than ^{209}Bi are unstable. Unstable nuclides lying below the line of stability are said to be *neutron deficient* or *proton rich*; those above the line are *neutron rich* or *proton deficient*. Unstable nuclides generally undergo transformations into those species lying closer to the line of stability. In the radioactive decay of nuclides, the initial unstable nucleus is called the *parent*; the final, more stable nucleus is termed the *daughter*.

F. Nuclear Transmutation

There exists a semiempirical mass formula that can be used to determine the mass of a nucleus. This formula is derived from a *liquid drop model* of the nucleus. This model explains nuclear-binding-energy increases and decreases in terms of factors such as the size and surface area of the nucleus, the Coulomb repulsion of the protons in a nucleus, the symmetry term favoring equal number of neutrons and protons, the pairing effect of nucleons, and the shell term or proximity of N or Z to magic numbers. The shape of the resulting semiempirical mass formula is parabolic as a function of Z . That is, if you plot atomic mass versus Z for isobaric nuclides, it follows a parabola, as depicted in Figure 3. The lower the mass of the isobar along this empirical curve, the more stable that nuclide, and nuclear transformations take the nuclides from higher to lower mass positions on this mass curve. These transitions occur through nuclear *beta* (β) *decay*, of which *electron* (β^-), *positron* (β^+), and *electron capture* (EC) decay are examples. In electron or positron decay, the charged particle is spontaneously created in and ejected directly from the nucleus. In electron capture, an electron is captured from an inner atomic shell. Because these decays result in changing the atomic number Z by 1 (see Figure 3), different chemical

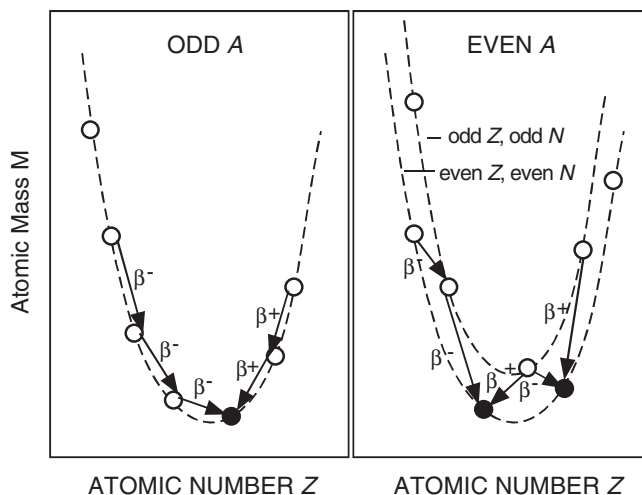


FIGURE 3 Depiction of isobaric mass parabola for odd- A (left) and even- A (right) nuclei. Open and filled circles represent unstable and stable nuclides, respectively. Transformations (represented by arrows) from lower to higher Z occur through β^- decay. Those from higher to lower Z are by β^+ or electron-capture decay (only β^+ is shown). (Adapted from Meyerhof, 1967.)

elements result, and a nuclear *transmutation* has occurred. Examples of decay by β^\pm emission or electron capture are given in Section IIB of this chapter.

The isobars with masses on the left of the parabola minimum are neutron rich (lie above the curve of stability) and are candidates for β^- decay. Those with masses to the right of minimum are proton rich (lie below the stability curve) and will undergo positron decay or electron capture. The isobar with the lowest mass on the parabolic curve is the most stable. It turns out that the minimum of this curve as a function of A follows the exact shape of the empirical line of stability. The deviation of the stability line from $N = Z$ or $Z = A/2$ is caused by the competition between the Coulomb energy, which favors $Z < A/2$ (more neutrons than protons) and the N – Z asymmetry energy which favors $N = Z$ or $Z = A/2$.

For odd- A isobars, the pairing effect is negligible, and there is only a single mass parabola, and transitions occur from higher to lower positions along this curve. For even- A isobars, two closely lying mass parabolas are generated due to the different binding energies (and, hence, masses) of isobars with even- N and even- Z compared to those with odd- N and odd- Z , due to the significantly different pairing effects. In this case, transitions occur between isobars along both mass parabolas, as depicted in Figure 3.

G. Nuclear Decay Probability

If N_0 identical parent nuclei were present initially, the number N most probably surviving after a time t is given by:

$$N = N_0 e^{-\lambda t} \quad (2)$$

where λ is the *decay constant*. This exponential decay law is characterized by the fact that a constant fraction of radioactive atoms disappears in a given constant time interval. The corresponding probability that the nucleus has decayed is proportional to the number of *disintegrations* that have occurred after a time t , $N_0(1 - e^{-\lambda t})$, which is also the probability of populating states (metastable, excited, or ground) of the daughter nucleus. If a single nuclide can decay by more than one independent process, the probabilities of the individual decay modes are additive, and the λ in Eq. (2) would be interpreted as the sum of the decay constants of the individual decay modes.

The *half-life* $t_{1/2}$ of a radioactive decay is the time interval in which the original number of nuclei is reduced to one-half, which is determined by setting $N = N_0/2$ in Eq. (2) and solving for t :

$$t_{1/2} = 0.693/\lambda \quad (3)$$

The mean life τ is the average survival time of a radioactive nucleus:

$$\tau = \frac{\int_0^{\infty} tP(t)dt}{\int_0^{\infty} P(t)dt} = \frac{1}{\lambda} \quad (4)$$

where we have substituted Eq. (2) as the survival probability $P(t)$ in a time interval dt . The *activity* $A(t)$ is the rate of generation of radioactive decay particles and also follows the same exponential decay form:

$$A(t) = -\frac{dN}{dt} = \lambda N_0 e^{-\lambda t} = \left(\frac{dN_0}{dt}\right) e^{-\lambda t} \quad (5)$$

The basic unit of activity is the curie (Ci). 1 Ci = 3.7×10^{10} disintegrations per second (dis/s). The SI unit of activity is the becquerel (Bq). 1 Bq = 1 dis/s = 2.7×10^{-11} Ci.

II. RELEVANT MODES OF NUCLEAR DECAY FOR MEDICAL RADIONUCLIDE IMAGING

A. Isomeric Transitions: Gamma-Ray Emission

If a radioactive parent nucleus decays into an isomeric (metastable) rather than excited state of the daughter, the decay of the daughter is an *isomeric transition*. This isomeric decay can result in the emission of a gamma ray (γ -ray) or ejection of an internal conversion electron. These transitions do not involve a change in the atomic number Z , and so the parent and daughter are chemically identical. If the energies of the metastable and ground states are E_i and E_f , respectively, the gamma ray is emitted with the full

transition energy $\Delta E = E_i - E_f$. The internal conversion electron is ejected with a kinetic energy:

$$T_e = E_i - E_f - E_b \quad (6)$$

where E_b is the binding energy of the electron in the atomic shell from which it has been ejected and the recoil energy of the atom has been neglected. Internal conversion should be viewed as an alternative and independent process by which a nucleus can release excitation energy besides gamma-ray emission. The likelihood of this process to occur instead of gamma emission increases with higher Z and lower ΔE . Using quantum mechanics terminology, internal conversion is also more likely to occur for inner atomic shell electrons (K , L , M , N) due to the more significant overlap of the inner atomic shell and nucleon *wave functions*. The two K -shell electrons' wave functions have the largest overlap with the nucleus. It should be noted that because the atom is left in an excited state of energy E_b , internal conversion is always accompanied by a secondary process by which the atomic excitation energy is released through X-ray or Auger electron emission (with net energy release E_b). This secondary process is discussed again in a subsequent section. For an in-depth discussion of the classification of gamma-ray emissions in terms of nuclear *spin* and *parity* states, angular momentum carried off by the *multipole radiation moments*, and the associated *selection rules* for transitions, see Meyerhof (1967) and Evans (1972).

Gamma-ray emission from typical short-lived nuclear deexcitation is of little use for imaging. Because of their relatively long *lifetimes*, metastable radionuclides are important to nuclear emission imaging. If the *half-life* of the decay is anywhere from a few minutes to a few months, the isomeric gamma-ray emissions can be used for *in vivo* imaging. Figure 1 highlights the isomeric decay scheme of ^{99m}Tc that leads to the well-known 140-keV photon emission that is favorable for use with a gamma-ray camera. This emission has a reasonable half-life (6 h), delivers a relatively low radiation dose, and the isotope can be used to label a wide variety of imaging agents. The internal conversion electrons, however, cannot be imaged *in vivo* with radiation detectors positioned outside the body due to the rapid absorption of electrons in tissue. We discuss the absorption of charged particles in matter later in this chapter and in Levin *et al.* (Chapter 16 in this book).

B. Isobaric Transitions: Beta (β) Emission

Beta (β) decay is a process by which a neutron n in a nucleus is transformed into a proton p , or vice versa, involving the spontaneous emission or absorption of a β particle (electron, e^- or positron, e^+) and electron neutrino (ν_e , or anti-neutrino, $\bar{\nu}_e$) within a nucleus. There are four processes that are all considered forms of β decay from parent (P) into daughter (D) nuclei:

$P(A,Z) \rightarrow D(A,Z+1) \quad n \rightarrow p + e^- + \bar{\nu}_e$ (electron emission)

$P(A,Z) \rightarrow D(A,Z-1) \quad p \rightarrow n + e^+ + \nu_e$ (positron emission)

$P(A,Z) \rightarrow D(A,Z-1) \quad e^- + p \rightarrow n + \nu_e$ (electron capture)

$P(A,Z) \rightarrow D(A,Z-1) \quad \bar{\nu}_e + p \rightarrow n + e^+$ (inverse beta decay)

Because the atomic number Z changes by 1 in beta decay, parent and daughter nuclei correspond to different chemical elements and a transmutation of elements has occurred. Note that in β decay, because the mass number A does not change, the parent and daughter are always isobars.

In principle, decay by electron emission can originate from within the nucleus or for a free, unbound neutron. However, because the mass of the neutron ($939 \text{ MeV}/c^2$) is slightly larger than that of the proton ($938 \text{ MeV}/c^2$), decay by positron emission occurs only from within a nucleus, which supplies the necessary energy. Energetically, ignoring the recoil energy of the daughter nucleus, for isobars with atomic mass $M(A,Z) > M(A,Z+1)$, electron decay takes place from Z to $Z+1$ (see Figure 3). Pure β^- emitters include ${}^3\text{H}$, ${}^{14}\text{C}$, and ${}^{32}\text{P}$.

For those nuclei with $M(A,Z) > M(A,Z-1) + 2m_0$ (m_0 = electron rest mass), positron decay can take place from Z to $Z-1$ (see Figure 3). Note that this $2m_0$ term comes about because we have written the inequality in terms of atomic rather than nuclear masses. After ejection from the nucleus, the positron loses its kinetic energy in collisions with atoms of the surrounding matter and comes to rest. In tissue, this occurs typically within a few millimeters from its point of emission and within a nanosecond. Near or at the point at which the positron stops, it combines with an atomic electron of the surrounding material and, as is typical for the union of particle and antiparticle, *annihilation* occurs. The annihilation probability is greatest for very slow positrons. In this annihilation reaction, the mass energy of the electron–positron system at or near rest ($2m_0c^2 = 1022 \text{ keV}$) is converted into electromagnetic energy (photons) called *annihilation radiation*. If the positron annihilates with a free electron, conservation of linear momentum requires that at least two photons be emitted. It is roughly a factor of 1000 more likely for two rather than three photons to be emitted. For the two-photon process, each has an energy equal to 511 keV and is oppositely directed (180° apart) from the other. If the electron is bound in an atom, annihilation with the production a single photon can occur because the atom can take up the necessary momentum, but this is an extremely rare process. Example positron emitters are ${}^{11}\text{C}$, ${}^{13}\text{N}$, ${}^{15}\text{O}$, and ${}^{18}\text{F}$.

EC is analogous to positron decay except an atomic electron is captured by a proton within a nucleus resulting in the emission of a neutrino. The most probable capture is from the atomic K shell (two electrons) because a K -shell

electron has the greatest probability of being inside the nucleus. In quantum mechanics terms, the K -shell electron wavefunction has largest overlap with that of the nucleons, similar in concept to the preference of the K -shell electrons for internal conversion of a nucleus. If $M(A,Z)c^2 > M(A,Z-1)c^2 + E_b$, (E_b = binding energy of the missing electron in the daughter nucleus) electron-capture decay can take place from Z to $Z-1$. For the much less probable valence electron capture, $E_b \approx 0$. Electron capture from an inner atomic shell is followed by a secondary process in which the available energy associated with filling the resulting orbital vacancy is carried off by the emission of X-rays or Auger electrons from the daughter atom. Example electron capture radionuclides are ${}^{57}\text{Co}$, ${}^{67}\text{Ga}$, ${}^{111}\text{In}$, ${}^{123}\text{I}$, ${}^{125}\text{I}$, and ${}^{201}\text{Tl}$. In some cases, EC competes with positron emission to decrease the atomic number by 1 and produce a more stable configuration. It turns out that EC is more frequent for heavier elements because it is more likely for their inner shell electrons to be closer to the nucleus at any given time.

Inverse beta decay occurs because neutrinos have a very small, but finite, weak interaction probability with nuclei (typically $\sim 10^{-14}$ – 10^{-19} smaller than for strong interaction *cross sections*). Unlike the other forms of beta decay, this reaction requires an external beam of neutrinos and thus is not relevant to medical nuclear emission imaging. In theory, this reaction is essentially the inverse of ordinary neutron beta decay because the creation of an electron is identical to the disappearance of a positron. Such a process can occur energetically if $M(A,Z) > M(A,Z-1)$.

Figure 1 depicts the *decay scheme* of the parent ${}^{99}\text{Mo}$ into the daughter ${}^{99\text{m}}\text{Tc}$ that occurs through β^- emission. The line representing the parent in a decay scheme is above and to the left of the daughter nucleus. The decay proceeds from left to right for β^- decay because the atomic number Z increases by 1. For β^+ emission, electron capture, and inverse beta decay, the decay proceeds from right to left because Z decreases by 1. Figure 4 shows the β^+ decay schemes of ${}^{11}\text{C}$, ${}^{13}\text{N}$, ${}^{15}\text{O}$, and ${}^{18}\text{F}$. The vertical distance between the lines represents the total amount of energy released (the transition energy) for the decay process and is also known as the *Q value*.

β decay can transform the parent into an excited, metastable, or ground state of the daughter. For the ${}^{99}\text{Mo}$ – ${}^{99\text{m}}\text{Tc}$ pair (Figure 1), both the metastable and excited states are formed from β^- decay. If an excited state is formed, the daughter nucleus promptly decays to a more stable nuclear arrangement by the emission of a γ -ray. This sequential decay process is called a β – γ *cascade*. The γ transition may be to another lower excited state and additional γ -rays may be emitted before the ground state is reached. This is known as a gamma-ray *cascade*. The sum of all the resulting gamma-ray, beta, and neutrino energies emitted is equal to the full transition energy between parent

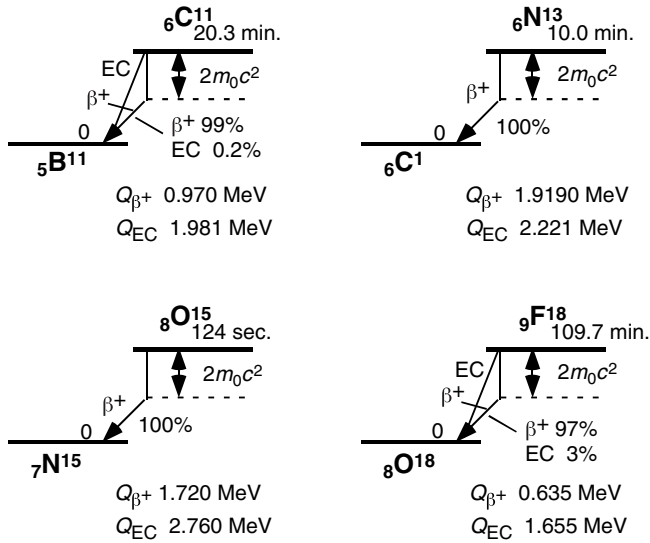


FIGURE 4 Decay schemes of common β^+ emitters. Q_{β^+} and Q_{EC} represent the total energy available to positron and electron capture decays, respectively. The maximum available energy for β^+ decay is the full transition energy from parent to daughter minus twice the electron rest mass (1.022 MeV). (Adapted from Lederer *et al.*, 1967.)

and daughter nuclei. Other example radionuclides that involve β - γ cascades are ${}^{131}\text{I}$, ${}^{133}\text{Xe}$, and ${}^{137}\text{Cs}$.

Note that the energy released in electron or positron decay is randomly shared between the β particle and the neutrino. Maximum β emission energy is equal to the full transition energy. This occurs when the neutrino is ejected with negligible kinetic energy, which is highly unlikely. For *allowed transitions*, where zero orbital angular momentum is carried off by the β - ν system, the theoretical distribution of energies or *energy spectrum* for betas is of the form (Wu and Moskowsky, 1966):

$$N(E)dE = gF(Z, E)pE(E_{\text{max}} - E)^2 dE \quad (7)$$

where, $N(E)$ = number of decays at energy E , E = total β energy in units of mc^2 , E_{max} = maximum (end-point) energy of the β particle in units of mc^2 , p = momentum of β in units of mc , g is a coupling constant, $F(Z, E)$ = Fermi function, and Z = atomic number of β decay daughter. The Fermi function takes into account the Coulomb interaction between the β and the daughter nucleus. A nonrelativistic approximation for $F(Z, E)$, valid for allowed transitions of lighter elements (Wu 1966; Daniel 1968) is:

$$F_{\text{allowed}}(Z, E) = 2\pi\eta / (1 - e^{-2\pi\eta}) \quad (8)$$

with $\eta = \pm Z\alpha E/p$ for β^{\mp} decay, and $\alpha = 1/137$ is the fine structure constant. The typical short-lived radionuclides used in nuclear medicine undergo allowed transitions.

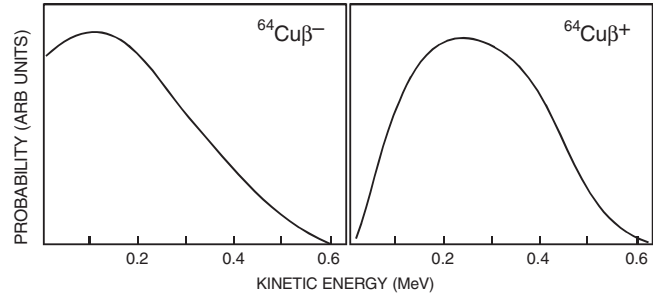


FIGURE 5 Depiction of kinetic energy spectra for β^- and β^+ emission of ${}^{64}\text{Cu}$. Adapted from Meyerhof (1967).

Because of the opposite charge of the electron and positron, the shapes of their energy spectra differ significantly. This is illustrated best for a nucleus that undergoes both β^- and β^+ decay modes. Figure 5 depicts the electron kinetic energy spectra for β^- and β^+ decay of ${}^{64}\text{Cu}$. The *end-point energy* or maximum β emission energy for the two modes are similar (0.58 MeV for β^- , and 0.65 MeV for β^+), but the lower energies are enhanced for the β^- and higher energies are favored for the β^+ . These effects are caused by nuclear Coulomb effects; the negatively charged electron is actually somewhat held back by the electric field of the nucleus, limiting the range of velocities; the positively charged positrons are repelled by the same electric field that facilitates acceleration of the particles leaving the nucleus. For an in-depth discussion of the classification of beta-ray emissions in terms of nuclear *spin* and *parity* states, angular momentum carried off by the β - ν pair, and the associated *selection rules* for transitions, see Meyerhof (1967) and Evans (1972).

Because electron decay and internal conversion both result in the ejection of an electron from the nucleus, initial investigations confused the two processes. Chadwick (1914) distinguished the two by demonstrating that the former has a continuous energy distribution for a given nuclide (Figure 5) and the latter is monoenergetic, as can be seen from Eq. (6). Gamma rays are also emitted with discrete energy values that are characteristic of the excitation energies of the radionuclide.

The neutrino is a particle with immeasurable mass and charge that was first postulated to exist by Pauli (1934) to explain the continuous energy distribution of electrons seen in electron decay without violating the laws of energy, momentum, and angular momentum conservation. The neutrino interacts only through the weak force, and so all the β decays are due to small perturbations of weak (as opposed to strong) or electromagnetic interactions within the nucleus. In elementary particle theory, nucleons comprise fundamental particles called *quarks* and these weak interaction decays are considered to occur between individual quarks. Whether a neutrino or antineutrino is

emitted in a decay is determined by another fundamental particle law known as *lepton number conservation* in which electrons and neutrinos are assigned a lepton number of +1 and their antiparticles are assigned a value of -1. The chargeless and essentially massless neutrinos and antineutrinos can be distinguished experimentally because the former have their intrinsic spins oppositely directed to the direction of travel, whereas the latter have their spins in the direction of travel.

III. PRODUCTION OF RADIONUCLIDES FOR IMAGING

Radionuclide imaging requires appropriate radioactive emissions. Naturally occurring radionuclides are not useful for tracers in biomedical diagnostic imaging because they are typically slowly decaying, long-lived constituents of heavy elements. The radionuclides used in nuclear medicine require some sort of artificial step in production that usually involves the bombardment of stable nuclei with subnuclear particles. The resulting *nuclear reactions* convert stable nuclei to higher-atomic-mass radioactive species that can be used directly to label compounds for imaging or for further generation of a desired imaging isotope. Nuclear reactions involve a bombarding particle a , target nucleus X , and the production of two products, a light reaction product b and heavy reaction product Y . Such a reaction is written as $a + X \rightarrow b + Y$, or in shorter notation $X(a,b)Y$. In this section we describe some basic methods and principles for radionuclide production for nuclear emission imaging. We define a produced radioactive sample that does not contain stable isotopes of the desired radionuclide to be *carrier free*. The ratio of sample radionuclide activity to the total sample mass is the *specific activity*. Obviously those samples with high specific activity and that are carrier free are most desirable for tracer imaging. In the next subsections we discuss the three most common methods for medical radioisotope production.

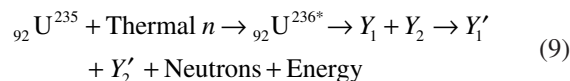
A. The Nuclear Reactor

1. Nuclear Fission in a Reactor

A nuclear reaction $X(a,b)Y$ is called fission if b and Y have comparable masses. Some nuclei fission spontaneously. Typically fission occurs only when sufficient energy is given to a nucleus by bombardment with subnuclear particles, such as neutrons, protons, or gamma rays, or by *capture* of a slow neutron. The common fissionable material used in a nuclear reactor is uranium isotopically enriched in ^{235}U content. ^{235}U undergoes spontaneous nuclear fission ($t_{1/2} \sim 10^9$ years) into two lighter nuclei or *fission fragments*. In the process, two or three prompt

fission neutrons are also released. The total energy released per nuclear fission is approximately 200 MeV, which goes mostly into the kinetic energy of the fission fragments and the neutrons emitted. These fission products are of use in radionuclide imaging. The radioactive fission fragments can be used in tracers or the neutrons released can be used for further radionuclide production through *neutron activation*. The fission fragments are not stable because in the fission process both fragments keep the same N/Z ratio as the original nucleus, which lies close to the stability line. The fragments are very neutron rich and prompt neutron emission is probable. Also, the neutron-rich (lying above the line of stability) fragments will eventually undergo β^- and gamma decay to take them closer to the stability line.

The spontaneous fission of ^{235}U is not a useful source of energy or neutrons. The fission neutrons emitted, however, can stimulate additional fission events when they bombard ^{235}U and ^{238}U . The most important reaction typically for a reactor is:



where the compound nucleus $^{236}\text{U}^*$ created is highly unstable and promptly decays in a manner independent of its mode of formation into the two fission products Y_1 and Y_2 . The fission products have the same N/Z ratio as ^{236}U and undergo prompt neutron emission and β^- and γ -ray decay to a more stable configuration for the final fission products Y_1' and Y_2' . All the elements near the center of the periodic table can appear as fission fragments, but fragments with mass numbers near 90 and 140 are more probable. For ^{235}U , example fission fragments are ${}_{42}\text{Mo}^{101}$ and ${}_{50}\text{Sn}^{133}$ with an average of 2.5 prompt neutrons ejected. The total energy release (~ 200 MeV) for the final fission products includes the energy carried off by neutrons, the energy release by β s, γ s, and ν s, and thermal energy, and is fairly independent of the pair of fission fragments.

2. Nuclear Reactor Design

The goal of a reactor is to provide a controlled fission *chain reaction* involving the sequential absorption of fission neutrons ejected in the reaction of Eq. (9). The reactor core contains a critical amount of fissionable ^{235}U and ^{238}U in fuel cells. In order to use fission neutrons efficiently to initiate further fission events, they must be slow or *thermal neutrons*. A moderator material, typically containing deuterium and graphite, surrounds the fuel cells and functions to slow down the prompt fission neutrons ejected from the cell. Rather than having one large fuel cell, in order to control the amount of sequential fission occurring, parallel control rods either shield or expose several small, parallel, rod-shaped fuel cells from one another. These control rods contain materials that have a high neutron

capture cross section. For control of the reaction it is desired that each fission event stimulate no more than one additional fission event. The fuel cells and control rods are correctly positioned so as to establish the critical conditions for a controlled chain reaction. Much of the energy release in a reactor is ultimately dissipated in the form of thermal energy. Reactor *meltdown* occurs when the positioning of these components is incorrect, causing multiple fission events to be initiated for each fission event. For safe containment and to control the temperature, the reactor core sits inside a high pressure vessel with coolant circulating throughout the volume. The entire vessel is surrounded by neutron and gamma-ray radiation shielding. The vessel also has pneumatic lines for insertion of target samples for production of radionuclides.

3. Reactor-Produced Radionuclides

a. Reactor-Generated Neutron Activation

Reactor-generated neutrons can also be used for production of radionuclides through *neutron activation*. Target nuclei sitting in a reactor core may capture neutrons and produce useful radioactive product nuclei through (n,p) and (n,γ) reactions. In the (n,p) reaction, the target nucleus captures a neutron and promptly releases a proton, transforming the target to a different chemical element. The isobaric product is carrier free and of high specific activity. In the (n,γ) reaction, the target nucleus captures a neutron and is converted into an excited state of the product nucleus, which on deexcitation promptly emits a gamma ray. For an (n,γ) reaction the target and product are the same chemical element (isotopes). Most reactor-produced radionuclides are of the (n,γ) variety. However, the products so produced are not carrier-free because they are the same chemical element as the target material and are of lower specific activity than radionuclides produced by fission products or fast neutron bombardment. Because neutrons are added to the target nuclides, the products lie above the line of stability and will tend to decay by β^- emission. Example important reactor-produced (n,γ) reactions are $^{50}\text{Cr}(n,\gamma)^{51}\text{Cr}$, $^{98}\text{Mo}(n,\gamma)^{99}\text{Mo}$, $^{124}\text{Xe}(n,\gamma)^{125}\text{Xe} \rightarrow ^{125}\text{I}$, and $^{130}\text{Te}(n,\gamma)^{131}\text{Te} \rightarrow ^{131}\text{I}$. ^{99}Mo is of special interest because it is the parent precursor for the $^{99\text{m}}\text{Tc}$ nuclear generator. The ^{99}Mo - $^{99\text{m}}\text{Tc}$ generator is discussed in the next section.

The activity produced when a sample is irradiated by a beam of particles depends on the intensity of the beam (Number of particles/Area/Time), the number of target nuclei in the sample that is seen by the beam, and the probability of interaction of the bombarding particle with a target nucleus. Probabilities for interactions in nuclear reactions are expressed in terms of the cross section. The cross section has units of area (barns; 1 barn = 10^{-24} cm²) and represents an effective area presented by a target nucleus in the path of the bombarding particle beam. It is a

fictitious area that is not necessarily related to the cross-sectional area of the struck nucleus. A nucleus may present a large area for one type of reaction and a small area for another. Because of their importance in radionuclide production, cross sections for thermal neutron capture have been extensively measured. The interaction cross section depends on the type and energy of the incoming particles and the type of interaction occurring. For example, the probability of neutron absorption or neutron capture cross section is highest for thermal neutron velocities. Neutron fluxes ranging from 10^{10} to 10^{14} neutrons/cm²/s (depending on the position within the reactor) are available. Even with intense neutron fluxes, only a small percentage ($\leq 0.0001\%$) of the target nuclei are activated. Thus, activation by (n,γ) tends to produce low specific activity samples because of the presence of significant nonactivated target material.

Using classic arguments, we can arrive at a simple expression for the number of activations produced per area per time. Assume a uniform beam of cross-sectional area A consisting of I neutrons/cm²/s bombards a very thin target sample (no more than one target nucleus is struck by the same particle) with thickness Δx and number density n atoms/cm³, with an interaction cross section σ . We pretend that with each target nucleus there is an associated cross-sectional area σ seen by the incoming beam such that if the center of a bombarding particle strikes inside σ there is a hit and a reaction is produced, and if the center misses σ no reaction is produced. Then the number of target activations per second per square centimeter, N , is equal to the number of particles removed from the beam per square centimeter of beam area per second, ΔI , due to interactions with target nuclei (assume isotropic distribution). The probability that any one incoming particle has a hit is equal to N/I and is also equal to the projected total cross section of all target nuclei ($nA\Delta x\sigma$) lying within the area of the beam divided by the total beam area A :

$$N/I = -\Delta I/I = n\sigma\Delta x \quad \text{or} \quad N = n\sigma\Delta x I \quad (10)$$

In addition to this constant rate of production of the sample, the product will also be continually decaying as well, so Eq. (10) also includes an exponential decay term. The product activity starts at zero and gradually increases with irradiation time t until it reaches equilibrium, when the production rate equals the decay rate. This saturation rate is just equal to the final expression in Eq. (10). So the activation rate N as a function of time t is expressed as:

$$N(t) = n\sigma\Delta x I (1 - e^{-\lambda t}) \quad (11)$$

where λ is the decay constant of the product radioactive nucleus. Dividing Eq. (11) by the mass of the sample gives an expression for the specific activity as a function of irradiation time.

b. Reactor-Generated Fission Fragments

The fission products formed in a reactor are rich in neutrons and decay by sequential β^- emission. This series of transmutations produces high-specific-activity radioactive offspring that can also be used in nuclear medicine. A common example of a useful fission product is the ^{99}Mo parent precursor for the $^{99\text{m}}\text{Tc}$ nuclear generator; ^{99}Mo can also be obtained through (n,γ) activation, but this produces a lower specific activity. A problem with fission-produced ^{99}Mo is that it may be contaminated with other high-specific-activity fission products. The ^{99}Mo – $^{99\text{m}}\text{Tc}$ generator is discussed in the next section.

B. The Nuclear Generator

A radionuclide generator is a system that repeatedly produces and replenishes a sample of short-lived daughter nuclei from the decay of a long-lived parent. The apparatus allows the clean separation and extraction of the daughter from the parent. The expressions for the decay rate of the parent dN_p/dt and the accumulation and decay of the daughter dN_d/dt radionuclides are:

$$\begin{aligned} \frac{dN_p}{dt} &= -\lambda_p N_p \\ \frac{dN_d}{dt} &= \lambda_p N_p - \lambda_d N_d \end{aligned} \quad (12)$$

where λ_p and λ_d are the decay constants of the parent and daughter samples, respectively. Solving the first differential equation for N_p , substituting the result into the second, solving for N_d , and using the relation $A(t) = \lambda N(t)$ for the activity—see Eqs. (2) and (5)—we arrive at an expression for the activity of the daughter sample A_d as a function of time:

$$A_d(t) = A_d(0)e^{-\lambda_d t} + A_p(0) \frac{\lambda_d}{\lambda_d - \lambda_p} (e^{-\lambda_p t} - e^{-\lambda_d t}) \quad (13)$$

where $A_d(0)$ and $A_p(0)$ are the daughter and parent sample activities at time $t = 0$, respectively. If the daughter sample did not exist initially, $A_d(0) = 0$ and only the second term remains in Eq. (13). With $A_p(t) = A_p(0)e^{-\lambda_p t}$ and rearranging terms, we obtain:

$$A_d(t) = A_p(t) \frac{\lambda_d}{\lambda_d - \lambda_p} (1 - e^{-(\lambda_d - \lambda_p)t}) \quad (14)$$

In a radionuclide generator, the parent half-life is several times longer than that of the daughter. From Eq. (13) or (14) we see that the activity of the daughter sample first increases and, as the parent is decaying, eventually exceeds that of the parent. As time goes on, the daughter activity reaches a maximum and then starts to decrease and follow the decay curve of the parent. This equilibrium point at which the ratio of the decay rate of the daughter to that of the parent is constant is called *transient equilibrium*. At transient equilibrium, using Eq. (14), $\lambda_d \gg \lambda_p$ and large t , we obtain $A_d/A_p = \lambda_d/(\lambda_d - \lambda_p) = \text{constant}$. Note that if only

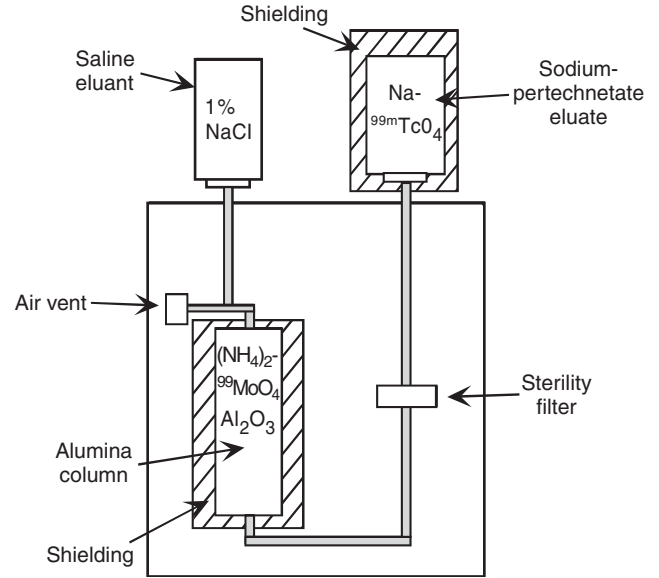


FIGURE 6 Schematic drawing of a ^{99}Mo – $^{99\text{m}}\text{Tc}$ generator. (Adapted from Rollo, 1977.)

a fraction of the parent atoms decay to the daughter, the daughter activity is given by Eq. (13) or (14) multiplied by that fraction. This is the case for the $^{99\text{m}}\text{Tc}$ – ^{99}Mo system in which this fraction or *branching ratio* is roughly 92%.

Because of the widespread clinical use of the isotope $^{99\text{m}}\text{Tc}$, the most important nuclear generator to nuclear medicine currently is the ^{99}Mo – $^{99\text{m}}\text{Tc}$ system. A cross section through a ^{99}Mo – $^{99\text{m}}\text{Tc}$ generator is schematically depicted in Figure 6. The generator is based on the concept of an ion-exchange column. The ^{99}Mo is absorbed onto an alumina (Al_2O_3) column in monovalent binding sites in the form of $(\text{NH}_4)_2^{99}\text{MoO}_4$ (ammonium molybdate). The ^{99}Mo in this compound exists in the form of the molybdate ion $^{99}\text{MoO}_4^{2-}$ in an ionic state of -2 units of charge. When ^{99}Mo in the molybdate ion decays, it is transformed into $^{99\text{m}}\text{Tc}$ in the form of the pertechnetate ion $^{99\text{m}}\text{TcO}_4^-$ in an ionic state of -1 . Because the $^{99}\text{MoO}_4^{2-}$ ion has two ionic charges it binds firmly to two binding sites on the alumina column, whereas the $^{99\text{m}}\text{TcO}_4^-$ ion with only one ionic charge weakly binds to only one site. Elution with isotonic saline solution (*eluant*) removes the weakly bound $^{99\text{m}}\text{TcO}_4^-$, leaving the $^{99}\text{MoO}_4^{2-}$ on the alumina column. The chemical form of the final solution (*eluate*) is $\text{Na}^{99\text{m}}\text{TcO}_4$ (sodium pertechnetate). This process of pulling saline solution through the alumina column into an evacuated vial for the extraction of the $^{99\text{m}}\text{Tc}$ is referred to as *milking* the generator. Roughly 80% of the available $^{99\text{m}}\text{Tc}$ activity is extracted in one elution. After elution, the $^{99\text{m}}\text{Tc}$ activity in the generator again grows with time. The time t_m at which maximum $^{99\text{m}}\text{Tc}$ activity is available is determined by setting $dA_d/dt = 0$ in Eq. (14), using $\lambda = \ln 2/t_{1/2}$, and solving for t :

$$t_m = 1.44 \frac{t_{1/2p} t_{1/2d}}{t_{1/2p} - t_{1/2d}} \ln \left(\frac{t_{1/2p}}{t_{1/2d}} \right) \quad (15)$$

Using $t_{1/2} = 6$ and 67 hours, respectively, for ^{99m}Tc and ^{99}Mo in Eq. (15), we arrive at roughly 24 hours for maximum available activity. Note that the maximum available ^{99m}Tc activity after elution as a function of time follows the decay curve of the original ^{99}Mo activity. Typical use of the generator involves repeated ^{99m}Tc buildup and elution phases until the ^{99}Mo decays away (~ 1 week).

One main problem with the ^{99}Mo - ^{99m}Tc generator is that there is a possibility that some ^{99}Mo is removed as well (^{99}Mo breakthrough) during elution due to imperfections in the production of the alumina column. This radionuclide impurity gives the patient unnecessary radiation exposure and will degrade the imaging performance due to a misrepresentation of the tracer distribution. The amount of this radionuclide impurity in the $\text{Na}^{99m}\text{TcO}_4$ sample can be assayed for by surrounding the vial with 5-mm-thick lead shielding and measuring its activity in a well counter. ^{99}Mo has high-energy gamma-ray emissions that will not be effectively stopped in the lead and will register activity, whereas the 140-keV ^{99m}Tc emissions cannot penetrate the lead. The Nuclear Regulatory Commission (NRC) limits for ^{99}Mo breakthrough are $1 \mu\text{Ci } ^{99}\text{Mo}/1 \text{ mCi } ^{99m}\text{Tc}$. The level of other radionuclide contaminants depends on the source of the ^{99}Mo . ^{235}U -fission-produced ^{99}Mo has the highest specific activity. However, the ^{99}Mo may be contaminated by other high-specific-activity fission products. ^{235}U -fission neutron-activated ^{99}Mo has lower specific activity but in general has lower amounts of radionuclide contaminants. Another concern is breakthrough of the Al^{3+} ion from the

alumina column. The presence of this aluminum ion can interfere with the labeling process and cause clumping of red blood cells. Chemical test kits are available that test for the presence of aluminum ion in the final solution. Current regulatory limits are $10 \mu\text{g Al}^{3+}/\text{ml Na}^{99m}\text{TcO}_4$.

C. The Cyclotron

A powerful method of radionuclide production is with the use of charged particle accelerators that bombard target samples with protons, deuterons (^2H nuclei), α particles (^4He nuclei), and other positively charged particles to produce useful nuclear reactions. However, unlike electrically neutral neutrons that are neither attracted or repelled by atomic nuclei during neutron activation of a target, charged particles have to overcome the repulsive nuclear Coulomb forces, or *Coulomb barrier*, before a nuclear reaction can occur. Thus, a relatively high energy particle beam of > 10 MeV is required. The most popular charged particle accelerator used in medicine is the cyclotron due to its relatively high compactness. Linear accelerators for medical isotope production are available as well but will not be discussed.

A schematic diagram of a cyclotron is given in Figure 7. The cyclotron comprises two hollow semicircular metal electrodes, referred to as Ds, with a narrow gap between them. The Ds are placed between the poles of a large DC electromagnet and are themselves connected to a high-frequency (~ 5 - to 10 -MHz) and high-voltage (~ 200 -kV AC) electromagnetic oscillator that produces a time-varying opposite electric polarity on the two Ds. A positive ion source near the center of the Ds is used to generate positively charged particles for acceleration in the

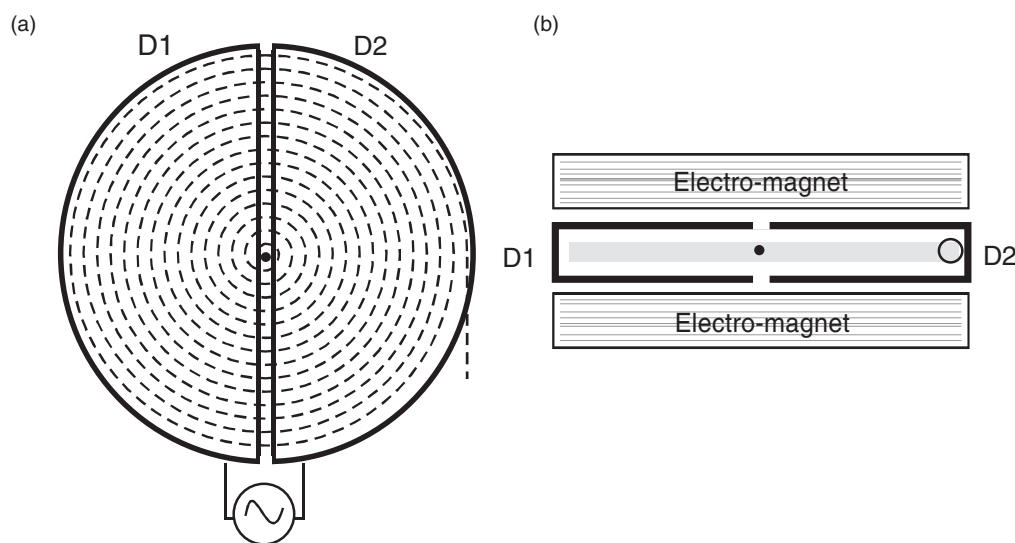


FIGURE 7 Schematic drawing of a cyclotron and the spiraling orbit of accelerated positive ions, (a) top view and (b) side view. Ions are injected into the cyclotron near the center of two D-shaped electrode shells. The Ds sit between poles of two electromagnets. The entire apparatus is evacuated.

cyclotron. For protons, a typical ion source consists of hydrogen gas irradiated by a beam of electrons produced from a tungsten filament. For deuterons or alpha particles, deuterium or helium gas, respectively, is used. During operation, the positive ions are created in bursts or pulses and injected into the center of the gap. Care must be taken to inject the ions at the exact center and in the same horizontal plane of the Ds. Once injected, the positive ions are immediately attracted toward the negative polarity D. As soon as the ions move, the magnetic $q\mathbf{v}\times\mathbf{B}$ force acts causing the ion group to follow a circular trajectory. As the curving ions approach the inside of the attracting D, because there is no electric field within the D the charge continues to move in the arc of a circle inside the D at constant speed until it again reaches the gap between the Ds. The AC frequency is tuned perfectly so that just as the particles emerge from the D, the Ds change polarity and the electric field is in the opposite direction and at its maximum amplitude. This causes the charged particles to accelerate toward the other D, which in the presence of the constant magnetic field causes the ions to move in a larger diameter circular orbit. The ions enter the second D with a larger velocity that remains constant until the particles curve around the other side and are again accelerated by the oscillating electric field. Each time the ions cross the gap, they gain energy qV where q is the ion charge and V is the voltage across the gap and the circular path diameter increases. The result is an outwardly spiraling accelerating path of the positive ions.

When the cyclotron is tuned perfectly, the increasing speed of the particles generated within the gap exactly compensates for the longer path traveled within a given D, and the ions continually arrive at the gap exactly in phase with the AC voltage. These conditions can be understood by considering the relevant force equations. A particle of charge q and mass m moving at velocity \mathbf{v} within the cyclotron under influence of a magnetic field \mathbf{B} experiences a force of magnitude qvB at right angles to the magnetic field and direction of its motion which is in the same plane as the Ds. This forces the particle into a circular orbit of radius r such that the centrifugal force equals the magnetic deflection force:

$$mv^2/r = qvB \quad (16)$$

The distance traveled while inside a D is $\pi r = \pi mv/qB$ and the time it takes is $\pi r/v = \pi m/qB$, independent of velocity as long as the charge to mass ratio of the accelerating particles and the magnetic field are constant. However, we know from special relativity that once particles are accelerated to relativistic velocities, the mass will change as a function of velocity, the time to traverse a D will change, the particle acceleration will no longer be in step with the AC voltage polarity switch, and the acceleration process is no longer efficient. For this reason,

the cyclotron in the form described here cannot be used to accelerate particles to ultra-high energies or to accelerate low mass particles, such as the electron (relatively little energy is required to take the electron to relativistic velocities).

When the radius of the ion orbit approaches that of the Ds, the particles can be directed onto a target placed either internally or externally by being deflected into a long and straight beam tube through a channel in one of the Ds. The energy available to charge particles in the cyclotron when the orbit radius reaches that of the Ds depends on the radius R of the Ds. From Eq. (16), the nonrelativistic velocity of a particle circulating at this radius is given by $v = qBR/m$. So the available kinetic energy E is:

$$E = q^2 B^2 R^2 / 2m \quad (17)$$

For a typical biomedical cyclotron magnetic field strength of 1.5 tesla, and a D radius of 40 cm, common achievable deuteron kinetic energies are approximately 10 MeV and those of alpha particles and protons are 15 MeV.

The positively charged accelerated particles hitting a target will add positive charge to the target nuclei and change their atomic number. The resulting cyclotron-activated product will tend to lie below the line of stability (see Figure 2) and decay by β^+ emission or electron capture. This is of interest for production of radioisotopes for positron emission tomography (PET). Four of the most commonly used PET isotopes ^{11}C , ^{13}N , ^{15}O , and ^{18}F may be produced in a cyclotron through (p,n) , (d,n) , or (α,n) reactions: $^{11}\text{B}(p,n)^{11}\text{C}$, $^{12}\text{C}(d,n)^{13}\text{N}$, $^{14}\text{N}(d,n)^{15}\text{O}$, and $^{20}\text{Ne}(d,\alpha)^{18}\text{F}$ (see Figure 4 for decay schemes). The products are usually carrier-free because the atomic number of the target nuclei changes, so high specific activities are available. The expression for activation rate for cyclotron-produced reactions is similar to that given in Eq. (11), except the charged particle activation cross sections and cyclotron beam intensities are in general lower than those available from reactor neutron activation and so cyclotrons produce less specific activity per irradiation time than reactors. The resulting target then undergoes further radiochemistry processing steps to produce the radiopharmaceutical.

IV. INTERACTIONS OF NUCLEAR EMISSIONS IN MATTER

We have seen that unstable nuclides that occur naturally or are artificially produced release energy in the form of photons or other particles. These emissions from a radioactive nucleus are too high in energy and too small in size to see by the naked eye. We therefore observe their existence and use their energy only through the effects they produce in matter. These effects are caused by the various

forces and interactions the nuclear emissions experience when they are confronted with the atoms and molecules of the material they traverse. Such processes are the basis of current radionuclide radiation detection and imaging devices and determine the efficiency and sensitivity of a detector. These reactions also may actually interfere with a measurement by disturbing the physical state of the radiation, causing, for example, deflection, absorption, or loss of radiation energy before detection is accomplished. Depending on the type of radiation, its energy, and the material in which it traverses, interactions may occur with the atom or nucleus as a whole or constituent particles such as electrons, neutrons, protons, and quarks. For radiation passing through matter at the relatively low energies of interest in biomedical radioisotope imaging, the most common interactions are electromagnetic in nature, involving the atom and nucleus as a whole as well as atomic electrons. In this section, we focus our discussion on the interactions of beta and gamma rays, the most commonly used forms of radiation in biomedical nuclear emission imaging. For the design and development of detectors in radioisotope imaging and for understanding how radiation interactions in the subject can effect imaging, it is important to understand how these emissions deposit their energy in matter.

A. Interactions of Electrons and Positrons in Matter

Betas encountered in radioisotope imaging either are directly emitted from positron or electron emitting nuclei or are ejected from atoms as a result of X-ray or γ -ray interactions. For the energies of interest in diagnostic biomedical radioisotope imaging, charged particles such as the electron or positron mainly lose energy and slow down through electromagnetic (Coulomb force) collisions with atoms and molecules. These interactions are characterized by both a loss of energy and deflection of the particle from its incident direction. These effects are primarily a result of multiple inelastic collisions with the atomic electrons of the material and elastic scattering from nuclei. Because these electromagnetic forces between the charged beta particles and the atoms in the material traversed are always present, the energy loss is a continuous process. Because the beta particle mass is equal to that of the orbital electrons with which it is interacting, large deviations in its path can occur through these collisions and a large fraction of its energy can be lost in a single encounter. So, a beta particle may not always slow down in a constant and continuous manner. Because the impulse and energy transfer for incident particles of equal mass are the same independent of charge, the energy loss, multiple scattering, and shape of the primary tracks are essentially identical for electrons and positrons of the same initial energy. Positrons, however, annihilate with

atomic electrons near the end of their trajectory, which leads to the emission of annihilation photons that will deposit energy far from the positron end point. For the beta energies of interest (10–1000 keV), the deflection of the electrons is due almost entirely to the elastic collisions with the atomic nuclei, while the energy loss (except that due to an effect known as Bremsstrahlung, which is practically negligible) results from the interaction with the atomic electrons. The result is a random zigzag, tortuous path for a beta particle as it slows down. Because the diagnostic energy range of interest is well below typical binding energies per nuclei, nuclear reactions in general will not occur as a result of beta interactions.

1. Radiative Energy Loss Effects

Rare energy loss effects that can occur in the common diagnostic emission imaging energy range of interest (≤ 511 keV) are the emission of Cerenkov radiation and Bremsstrahlung. *Cerenkov radiation* is a result of charged particles traveling faster than the speed of light in a medium, c/n , where c is the speed of light in a vacuum and n is the medium index of refraction. This phenomenon is an electromagnetic shock wave that results in the emission of a continuous frequency spectrum of polarized light that propagates at a fixed angle with respect to the direction of the particle.

Bremsstrahlung (German for “breaking radiation”) is the emission of a continuous spectrum of photon radiation energies due to the deceleration and deflection of the charge particle in the presence of the strong electric field of the nucleus. The loss of energy appears as a photon with energy equal to the difference between initial and final energies of the deflected beta particle. The Bremsstrahlung cross section σ_b , which gives the radiation emission probability, depends on the strength of the nuclear Coulomb force, which in turn depends on the atomic number and how close the encounter is. The Bremsstrahlung cross section varies as:

$$\sigma_b \sim Z^2 r_e^2 f(E) = Z^2 \left(\frac{e^2}{m_e c^2} \right)^2 f(E) \quad (18)$$

where Z is the nucleus atomic number, and $r_e \equiv e^2/m_e c^2$ is the classical electron radius = 2.82×10^{-13} cm. The function $f(E)$ is a strongly increasing function of initial energy E that becomes appreciable only for $E > m_e c^2$, the electron rest mass energy. The resulting average energy loss per length traversed in a medium due to the emission of Bremsstrahlung radiation varies as:

$$\left(-\frac{dE}{dx} \right)_{rad} \sim NE\sigma_b \quad (19)$$

where E is the incoming beta energy and N is the number density of atoms, $N = \rho N_a/A$ (ρ is density, N_a is Avogadro’s number, and A is atomic mass). Due to the $1/m^2$ and Z^2 dependence (Eq. 18), radiative energy loss

essentially only occurs for electrons and positrons and for high Z materials. It does not play a role in energy loss until the beta energy is high enough for the deceleration to be appreciable. At very high beta energies ($> 20 m_e c^2$ for lead and $> 200 m_e c^2$ for water) the energy loss is dominated by Bremsstrahlung. Figure 8a (later in the chapter) depicts the approximate radiation loss component of the beta energy loss per unit length as it traverses water and lead as a function of energy. In both media, the radiation loss is *negligible* for diagnostic energy ranges of interest (< 511 keV) for which the energy loss is almost entirely due to inelastic atomic collisions.

2. Inelastic Collision Energy Loss: Ionization and Excitation

The inelastic collisions with atomic electrons are mostly responsible for the energy loss of charged particles in matter. Energy is transferred from the particle to the atom causing ionization or excitation. Excitation is more probable than ionization, even at high energies. The ratio of probabilities of ionization to excitation and the average energy transferred to an ionized electron are nearly independent of the primary particle energy. Ionization and excitation can involve both inner and outer atomic shells of the atoms in the absorbing medium, but most of these inelastic collisions involve outer orbital electrons. If an inner-shell electron is ejected, an accompanying X-ray or Auger electron will also be emitted as a result of filling the inner-shell vacancy, as discussed in Section ID. Resulting ionization electrons typically have a mean kinetic energy of only a few electron volts. The maximum energy that can be transferred to a free atomic electron by a primary beta (electron or positron) is simply one-half the kinetic energy of the primary. Although the average energy transferred per inelastic collision is very small in comparison to the incoming particle's total kinetic energy, the typical number of collisions is large and a substantial cumulative energy loss is observed even in relatively thin layers of material. A charged particle continuously interacts with atomic electrons, and so the velocity continues to decrease (although not necessarily in a continuous manner) until the particle is completely stopped.

These atomic collisions are categorized as *hard* if the energy transferred is sufficient to produce an ionization, corresponding to a relatively close distance of approach with the atom. The collisions are *soft* if only an excitation results, corresponding to a not-so-close encounter and smaller energy losses than for ionization events. The energy transferred to an atom in excitation is dissipated in atomic and molecular vibrations and in the emission of low-energy radiation such as visible, ultraviolet, and infrared photons. In general, ionization electrons ejected will be rapidly absorbed. If the primary encounter is so hard that the energy transferred to the recoiling ionization

electron is sufficient for it to produce its own secondary ionization, this recoiling electron is termed a *delta* or *knock-on* electron.

Because the nuclear masses are much greater than those of incoming charged particles such as electrons or positrons, collisions with atomic nuclei are usually elastic in nature and the particle does not lose energy and is only deflected. Such collisions are termed *elastic scattering*. Elastic collisions with atomic nuclei occur less frequently than the inelastic interactions with atomic electrons.

The average energy lost per distance traversed by a beta particle dE/dx due to inelastic processes (ionization and excitation) is estimated by the Bethe-Bloch formula for betas (Leo, 1987; Knoll, 1989):

$$\frac{dE}{dx} = 4\pi r_0^2 \frac{mc^2}{\beta^2} NZ(A+B) \quad (20)$$

with

$$A = \ln\left(\frac{\beta\gamma\sqrt{\gamma-1}mc^2}{I}\right)$$

and

$$B = \frac{1}{2\gamma^2} \left(\frac{(\gamma-1)^3}{8} + 1 - (2\gamma^2 + 2\gamma - 1) \ln 2 \right)$$

where r_0 is the classical electron radius $= 2.82 \times 10^{-13}$ cm, $\gamma = (1 - \beta^2)^{-1/2}$, $\beta = v/c$, N is the number density of atoms for the medium (water-equivalent tissue, for example), Z is the atomic number, and I is the mean excitation potential of the medium in electron volts (which for $Z_{\text{eff}} < 12$ is approximately $I = 12Z + 7$; for water, assuming $Z_{\text{eff}} \approx 7.22$, $I \approx 94$ eV; Leo, 1987). This average energy loss includes both soft and hard collisions and excitation processes including emission of Cerenkov radiation (Leo, 1987). This expression essentially holds for both electrons and positrons. However, for incoming electrons the collisions are between identical particles, so the calculation of dE/dx must take into account their indistinguishability, which is unnecessary for incoming positrons. This leads to a different expression for the factor B for electrons and positrons. Fortunately, this difference is only slight for the energies of interest and we ignore it here.

The form of dE/dx for beta particles traversing lead as a function of their energy is shown in Figure 8a. There are a few features to note from Eq. (20) and Figure 8a. Because the terms A and B vary slowly with particle energy, the $1/\beta^2$ term dominates, especially for lower energies. This particular velocity dependence is due to the fact that the slower the incoming beta, the more time it spends in the vicinity of the atomic electron it interacts with and the relatively larger the momentum imparted to that electron through the Coulomb force. This transferred energy goes as the square of the momentum imparted. Near 500 keV, where the kinetic energy is of the order of the rest mass

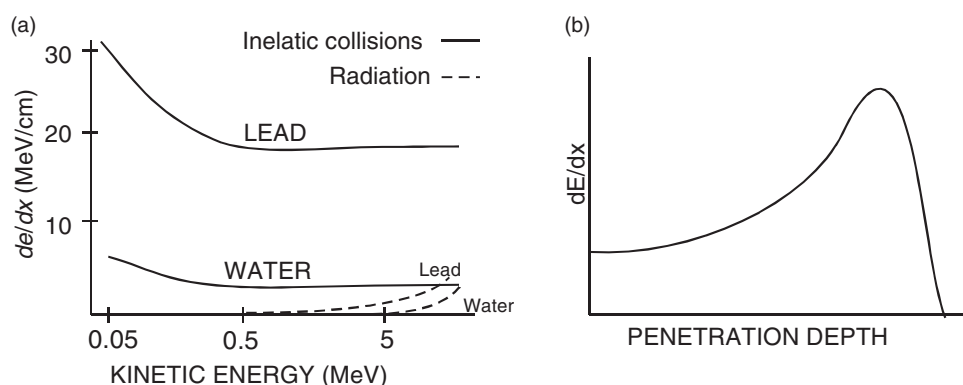


FIGURE 8 (a) Shape of inelastic collision energy loss per length dE/dx for betas as a function of kinetic energy. Also shown is the slight contribution due to radiative emission loss that becomes important only at very high energies. (Adapted from Leo, 1987; Knoll, 1989; Heitler, 1960; Siegbahn, 1955.) (b) Typical shape of Bragg curve for betas depicts the variation of dE/dx as a function of electron penetration depth in matter. The particle is more ionizing toward the end of its trajectory.

energy, the beta velocity approaches the constant speed of light and is relativistic enough for the factors A and B to have an effect, and the curve begins to level off. dE/dx reaches a minimum near 1 MeV ($v \sim 0.9 c$) where the beta is *minimum-ionizing*, the tracks are straighter, and the particle energy is absorbed less quickly through inelastic collisions with atomic electrons. Because the velocity asymptotically approaches a constant, so do the momentum imparted and the energy transferred to an atomic electron, and the energy loss per collision is approximately constant.

As the energy increases beyond the minimum, the $1/\beta^2$ factor approaches a constant value 1 and dE/dx begins to very slowly rise due to the logarithmic dependence of the factor A . The slight increase in inelastic collisional dE/dx after its minimum at higher energies for fast electrons is mostly due to the production of Cerenkov radiation. In dense media, however, this energy loss mechanism is partially compensated by a polarization effect for fast electrons, whereby some of the electronic charge is effectively shielded by polarization of the medium. This explains the almost insignificant increase of dE/dx in the high energy region for lead seen in Figure 8a.

Because dE/dx rapidly increases as the beta slows down, most of the energy deposited and the highest ionization density created along a beta track will be near its end. A depiction of the energy deposited per unit length for a charged particle as a function of penetration depth demonstrates this feature and is known as a *Bragg curve* (Figure 8b). Assuming the beta loses energy in many small, equal decrements per inelastic collision, this nonlinear energy deposition means that the maximum extent or *range* of the trajectory varies with energy in a nonlinear fashion. Because the spectrum of particle energies in beta decay is peaked toward lower energies, a significant fraction of beta trajectories will end in less than 0.5 mm. Because of the

dependence of dE/dx on the product NZ of the ionization medium, high-atomic-number, high-density materials will have the greatest stopping power. High-energy betas lose energy at a lower rate (see Figure 8a) and follow a straighter path than do lower-energy betas.

When dE/dx is expressed in terms of *mass thickness* (mg/cm^2) by dividing by the density ρ (mg/cm^3), it is found to vary little over a wide range of materials. This is due to the fact that the number of electrons per gram is nearly the same for all materials. Equation 20 applies to pure elements. For mixtures of n atoms an approximate expression for dE/dx can be found by averaging dE/dx over each element in the compound weighted by the fraction of electrons in each element. This is known as *Bragg's rule*:

$$\frac{1}{\rho} \frac{dE}{dx} = \frac{f_1}{\rho_1} \left(\frac{dE}{dx} \right)_1 + \frac{f_2}{\rho_2} \left(\frac{dE}{dx} \right)_2 + \dots + \frac{f_n}{\rho_n} \left(\frac{dE}{dx} \right)_n \quad (21)$$

where f_i is the fraction by weight of element i in the compound. This relation is another justification for expressing energy loss as mass stopping power $(1/\rho)(dE/dx)$, rather than linear stopping power dE/dx .

3. Hard Collisions: Knock-on (δ) Electron Production

The probability per unit length of emitting a delta ray of energy E_δ due to a beta particle with incident kinetic energy E (with $\beta = v/c$) traversing a medium of electron density N is given by (Ritson, 1961):

$$P(E_\delta) = \frac{2\pi r_e^2 m_e N}{\beta^2} \frac{1}{E_\delta^2} \quad (22)$$

where r_e is again the classical electron radius. The number of δ -rays, N_δ , created per unit length with energies greater than ϵ in an average track is obtained by integrating Eq. (22) over that energy range:

$$N_{\delta}(E_{\delta} > \varepsilon) = \frac{2\pi r_e^2 m_e N}{\beta^2} \frac{1}{\varepsilon} \quad (23)$$

4. Multiple Coulomb Elastic Scattering from Nuclei: Moliere's Theory

Because of the large mass of the nucleus compared to that of betas, the energy lost by betas in Coulomb collisions with nuclei is negligible, and the collisions are essentially elastic. However, because of the larger target mass, transverse elastic scattering of betas is appreciable in the Coulomb field of the nucleus. The electron and positron are also susceptible to *multiple scattering* or repeated elastic Coulomb scatters by nuclei, although with a smaller probability than for multiple inelastic collisions with atomic electrons. If the absorber is so extremely thin that the probability of more than one Coulomb scatter is small (as was the case with the well-known Rutherford experiment with alpha particles and a gold foil), then the angular distribution follows the Rutherford formula:

$$\frac{d\sigma}{d\Omega} = Z^2 r_e^2 \frac{mc / \beta p}{4 \sin^4(\theta/2)} \quad (24)$$

where Z is the atomic number of the nucleus, $\beta = v/c$ and $p = mv$ for the incoming beta particle, and θ is the scattering angle. Thus, most collisions cause only small angle deflections.

The Moliere theory of multiple Coulomb scattering is appropriate for most beta energies encountered in medical radioisotope imaging, where the number of elastic collisions with the nucleus of the absorber is greater than roughly 20 and includes the probability of large angle scatters and back scatters. Because of its small mass, a beta particle is susceptible to large angle deflections by scattering from nuclei. In fact, betas may be turned around and backscattered out of an absorber. This effect is particularly strong for low-energy electrons and increases with the Z of the material and angle of incidence. For independent multiple elastic scatters off of nuclei in the absorbing medium in which the number of collisions $\Omega_0 > 20$, a standard description is given by Bethe's (1953) treatment of Moliere's theory of multiple Coulomb scattering, which describes the scattering of fast-charged particles in a screened Coulomb field. In Bethe's work, the probability that an electron of momentum p and velocity v is scattered into the angle θ and angular interval $d\theta$ after traversing a thickness t in a material of atomic number Z and number density of atoms N is given by:

$$f(\theta) \theta d\theta = \lambda d\lambda \int_0^{\infty} y dy J_0(\lambda y) \exp\left[\frac{1}{4} y^2 (-b + \ln \frac{1}{4} y^2)\right] \quad (25)$$

where y is a dummy variable, J_0 is the zeroth-order Bessel function, $\lambda = \theta/\chi_c$, b is defined by

$$e^b = \frac{\chi_c^2}{1.167 \chi_a^2} \quad (26)$$

where χ_c characterizes the minimum single scattering angle possible,

$$\chi_c^2 = \frac{4\pi N t e^4 Z(Z+1)}{(pv)^2} \quad (27)$$

and χ_a parameterizes the screening angle, given in Moliere's approximation as

$$\chi_a^2 = \chi_0^2 (1.13 + 3.76\alpha^2) \quad (28)$$

where χ_0 represents the critical scatter angle below which differences from the Rutherford scattering law (with the characteristic $1/\theta^4$ dependence) become apparent due to nuclear effects; χ_0 is given by:

$$\chi_0 = \frac{\lambda'}{(0.885 a_0 Z^{-1/3})}, \quad (29)$$

$\alpha = Ze^2/hv$, $\lambda' = h/p$, the electron DeBroglie wavelength, h is Planck's constant, a_0 is the Bohr radius, J_0 is the zeroth-order Bessel function.

Bethe assumed $\chi_0 \ll \chi_c$ in the derivation of $f(\theta)$, which holds for relatively thick t , but fails for $y \sim \chi_c/\chi_0 \sim e^{b/2}$. The quantity $e^b \sim (\chi_c/\chi_a)^2$ is roughly the number of collisions Ω_0 that occur in the thickness t of material. To determine whether Moliere's theory of multiple scatter holds for a particular ionization medium, we check to see whether e^b is greater than 20. Moliere considered his model to be valid for $\Omega_0 > 20$ and when the parameter B (defined later) > 4.5 . For example, in water-equivalent tissue at room temperature, an 80-keV beta that travels a maximum distance of 0.14 mm from its point of emission has $\Omega_0 \approx 30$ and $B \approx 5$; so we expect Moliere's theory to apply. However, a 50-keV beta with a maximum range of 0.06 mm in water has $\Omega_0 \approx 20$, which is near the region where Moliere's theory breaks down. So we expect there to be a discrepancy between theory and measurement below 50 keV in water.

Moliere evaluated $f(\theta)$ for all angles by a change of variable $\vartheta = \theta/(\chi_c B^{1/2})$. B is a constant defined by: $b = B - \ln B$. With these definitions, $f(\theta)$ can be expanded in a power series in B^{-1} :

$$f(\theta) \theta d\theta = \vartheta d\vartheta [f^{(0)}(\vartheta) + B^{-1} f^{(1)}(\vartheta) + B^{-2} f^{(2)}(\vartheta) + \dots] \quad (30)$$

where

$$f^{(n)}(\vartheta) = \frac{1}{n!} \int_0^{\infty} u du J_0(u\vartheta) \exp\left(-\frac{u^2}{4}\right) \left[\frac{u^2}{4} \ln\left(\frac{u^2}{4}\right)\right]^n \quad (31)$$

where $u = B^{1/2} y$. In the limit of large angles, the distribution function tends toward the Rutherford single scattering law: $f_R(\theta) \theta d\theta = (2/B) d\vartheta / \vartheta^3$. The ratio of Moliere to Rutherford scattering probabilities is $R = f/f_R = 1/2 \vartheta^4 (f^{(1)} + B^{-1} f^{(2)} + \dots)$, which gives asymptotic expressions for f^1 and f^2 . Together with $f^{(0)}$ obtained from $f^{(n)}$ we have:

$$\begin{aligned}
 f^{(0)}(\vartheta) &= 2e^{-\vartheta} \\
 f^{(1)}(\vartheta) &= \frac{2(1-5\vartheta^{-2})^{-4/5}}{\vartheta^4} \\
 f^{(2)}(\vartheta) &= \frac{16(\ln \vartheta + \ln 0.4)}{\vartheta^6(1-9\vartheta^{-2}-24\vartheta^{-4})}
 \end{aligned}
 \tag{32}$$

For $\vartheta > 4$ (large θ) these expressions will hold. For $\vartheta < 4$ (small θ) we may use the values in Table II of Bethe (1953) to determine $f^{(1)}$ and $f^{(2)}$. For most calculations, it is not necessary to go past $f^{(2)}$.

It is difficult to use approximations for $f(\theta)$ that will hold for both small and large values of θ in multiple scatter calculations because it is not a simple function for the entire angular range of interest. In Monte Carlo simulation calculations of electron trajectories, we may use rejection techniques for generating $f(\theta)$ (Levin and Hoffman, 1999). Figure 9 shows the form of the distribution of scattering angles for multiple scattering of betas in water as estimated by incorporating Eqs. (25)–(32) into a Monte Carlo simulation (Levin and Hoffman, 1999). A vast majority of the collisions result in a small angular deflection of the particle. For small-angle scatters ($< 5^\circ$), this distribution is approximately Gaussian in form. For larger scattering angles, the deviation from a Gaussian is significant due to the possibility of single large-angle deflections. For small scattering angles, the multiple-scatter cross section is largest. In any given layer of material, the net elastic Coulomb scattering is mostly the result of a large number of small deviations, each independent of the others.

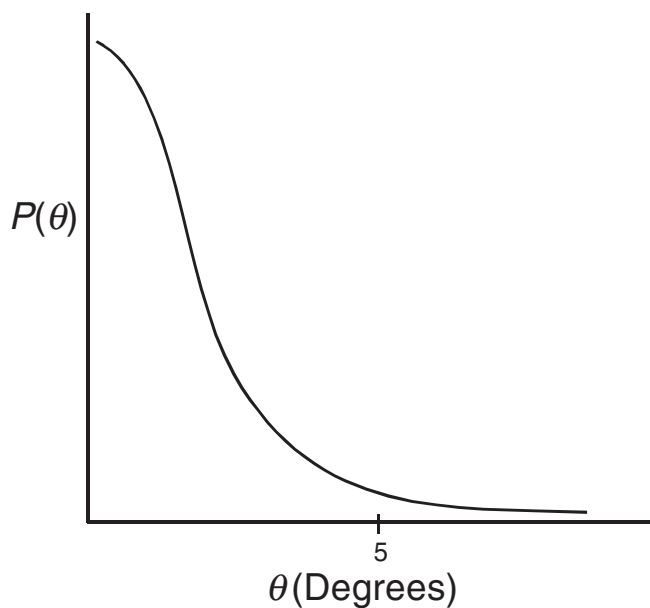


FIGURE 9 Form of the angular distribution for multiple scattering of betas in water.

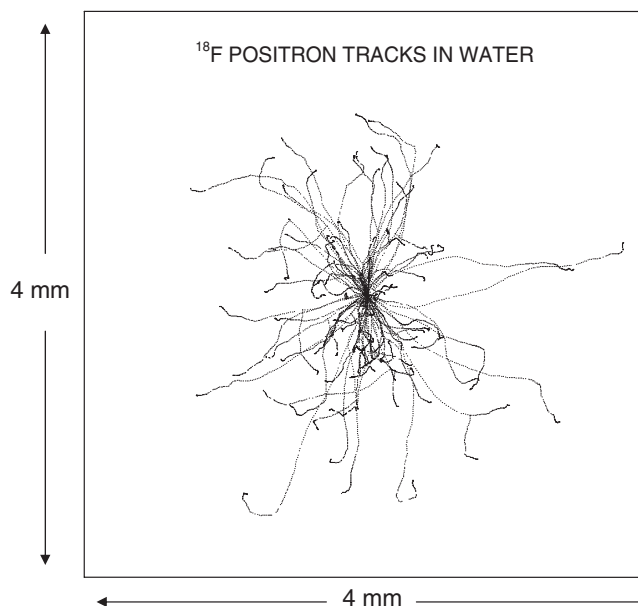


FIGURE 10 Projections onto the plane of 100 Monte Carlo calculated positron trajectories from a point source in water. (Adapted from Levin and Hoffman, 1999.)

Figure 10 shows projections onto a plane of 100 positron trajectories from a ^{18}F point positron source in water as calculated by a Monte Carlo simulation calculation (Levin and Hoffman, 1999) that incorporates the effects described in Eqs. (7)–(8) (beta decay energy spectrum), (20)–(23) (inelastic collisions: ionization, excitation, and delta electron production), and (25)–(32) (multiple Coulomb elastic scattering). The multiple scatter angle is inversely related to the energy. Thus, small-angle multiple scatter is dominant along the beginning of a track because at higher energies the scattering involves primarily small-angle deflections. Toward the end of the track where the energy is lowest, the scatter angle is largest. dE/dx also rapidly increases as the electron slows down. Thus, toward the end of the trajectory, scattering at large angles becomes more frequent and the electron's path begins to bend around and show more curvature or backscatter. This curving around for lower energies is most prominent for high Z materials. Note the signs of δ electron production along some of the tracks plotted in Figure 10. From conservation of energy and momentum, δ electrons are ejected at large angles from the primary track.

5. Range of Beta Trajectories

The *range* of a beta trajectory is defined as the maximum distance it penetrates before it loses all of its energy. In the case of beta decay where there is a continuous spectrum of possible energies, the range refers to the maximum distance penetrated for all possible beta decay energies. Note that the total path length traversed by the beta is considerably

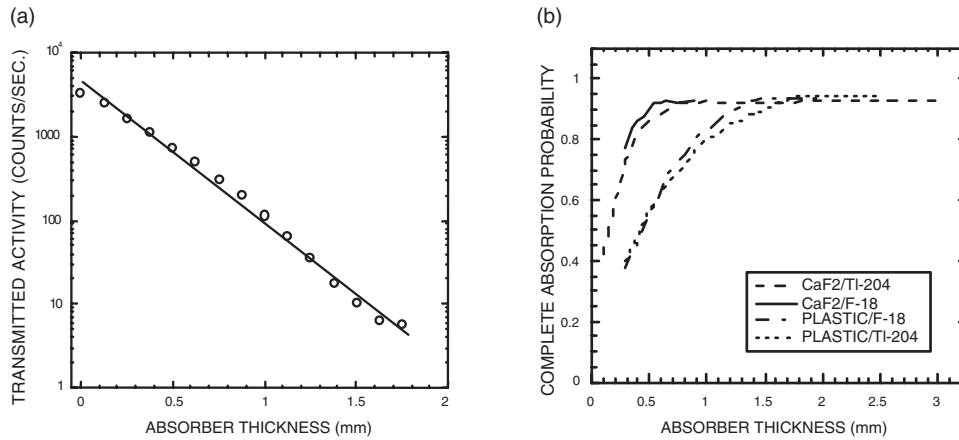


FIGURE 11 (a) Measured transmitted ^{204}Tl beta activity as a function of plastic absorber thickness. (b) Calculated probability for complete absorption of all beta tracks in $\text{CaF}_2(\text{Eu})$ and plastic beta detectors as a function of material thickness for ^{204}Tl and ^{18}F . (Adapted from Levin *et al.*, 1996.)

greater than the range as defined here. If the energy loss were a continuous process, this range would have the same well-defined value for particles of the same mass and initial energy for a given material traversed. In reality, the energy loss is not continuous but stochastic or statistical in nature and two identical beta particles with the same energy will not undergo the same number and type of collisions in a given medium. Because of multiple elastic scattering by nuclei, the range of betas is in general very different from the calculated path length obtained from an integration of the dE/dx formula. Energy loss by betas also has large fluctuations or *energy straggling* due to the large energy transfer collisions allowed. It is even possible for a few single collisions to absorb the major part of the electron's energy. This results in great variation in range or *range straggling* for betas. However, it is a fact that beta ranges expressed in grams per square centimeter are nearly identical for different materials.

Because of their continuous spectrum of energies, the absorption of allowed beta decay electrons and positrons as a function of absorber depth is well approximated by an exponential:

$$I = I_0 e^{-\mu x} \quad (33)$$

where I is the beta source intensity after a thickness x of the absorbing medium is traversed, I_0 is the initial intensity, and μ is the beta absorption coefficient, which is a function of the material and beta decay end-point energy. Figure 11a shows results from transmission-absorption measurements for a ^{204}Tl beta source ($E_{\text{max}} = 765$ keV) using plastic as an absorber medium. Thin plastic sheets were successively stacked and placed in between the source and a beta detector. The log of the transmitted activity as a function of absorber thickness follows a straight line, indicating that Eq. (33) is a good approximation for describing the absorption properties of beta source emissions. For this

measurement, we see that 1.7-mm of plastic stops nearly all ^{204}Tl betas. Figure 11b shows the results of a Monte Carlo calculation of the probability for complete absorption of all beta emissions from ^{204}Tl and ^{18}F in both plastic ($\rho = 1.19$ g/cm 3 , $Z_{\text{eff}} \approx 6.6$; close to absorption parameters of water) and $\text{CaF}_2(\text{Eu})$ ($\rho = 3.17$ g/cm 3 , $Z_{\text{eff}} \approx 16.9$), which are common beta scintillation detection materials, as a function of absorber thickness. Because the two beta sources have similar end-point energies, nearly all beta emissions from these sources are completely contained in approximately 1.8 mm of plastic and 0.7 mm of $\text{CaF}_2(\text{Eu})$. Note the probability for complete absorption of all tracks in Figure 11b never reaches 1 due to effects such as electron scatter out of the absorber and Bremsstrahlung. Figure 12 shows results from Monte Carlo simulations of ^{18}F beta point source interaction trajectories in $\text{CaF}_2(\text{Eu})$ from which the exponential form of absorption as a function of depth (Eq. 33) can be visualized. The corresponding positron energy spectrum is shown in the inset of Figure 12.

B. Interactions of High-Energy Photons in Matter

High-energy photons encountered in biomedical radioisotope imaging can be gamma rays resulting from nuclear deexcitation, annihilation photons resulting from positron annihilation, characteristic X-rays resulting from inner atomic shell transitions of atoms ionized by gamma- or beta-ray interactions, or Bremsstrahlung X-rays resulting from the deceleration of betas in the Coulomb field of the nucleus. Depending on the nuclear energy levels involved, the typical gamma-ray energies are larger than 100 keV. Annihilation photons carry away the mass-energy of the positron-electron system at rest, which means each has 511 keV. Characteristic X-rays typically have discrete energies under 100 keV, depending on the binding energies of the atomic shells involved. Bremsstrahlung X-rays

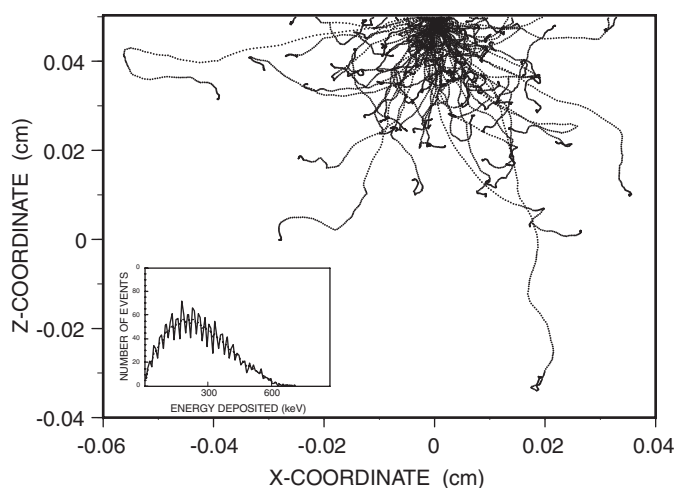


FIGURE 12 Results from Monte Carlo simulations of positron interaction trajectories in $\text{CaF}_2(\text{Eu})$. All interactions are shown for 100 positron events from an ^{18}F point source placed on top of the scintillator. Inset: Calculated spectrum of energies deposited in the crystal from 2500 ^{18}F positron events (fit to data is superimposed). (Adapted from Levin *et al.*, 1996.)

exhibit a continuous spectrum of energies up to a few hundred keV due to the nature of electro-magnetic collisions between betas and the nucleus. For the beta energies and materials of interest in nuclear medicine, Bremsstrahlung is not an important source of high-energy photons, as discussed in the previous section.

Because photons do not carry electric charge they interact differently with the molecules, atoms, electrons, and nuclei and with a lower probability than do beta particles. However, because photons carry the electromagnetic field, they will interact with electric charge. For the photon energies of interest in nuclear medicine, the interactions are mainly with individual atomic electrons. Unlike the nearly continuous Coulomb interactions that betas undergo as they traverse matter, high-energy photons lose their energy to the individual atomic electrons discretely. Once energy is transferred to an individual atomic electron, that charged particle traverses matter as described in the previous section. The two main interactions with individual atomic electrons high energy-photons experience for the energies of interest are the Compton effect and the photoelectric effect.

1. Compton Effect

If the incident photon energy and momentum are, respectively, much larger than the binding energy and momentum of a struck electron, then for purposes of calculations, the electron can be considered approximately unbound (free) or loosely bound and at rest. From energy and momentum conservation considerations, because the photon is massless and the electron is not, a photon cannot be completely absorbed by and transfer all of its energy to a

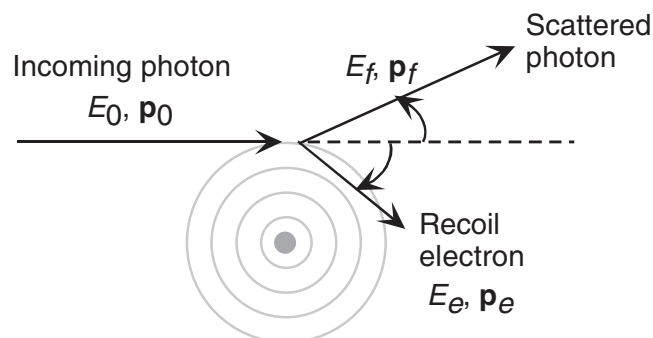


FIGURE 13 Depiction of the two-body Compton scatter process in the plane that probably involves outer-shell electrons.

loosely bound electron at rest. Therefore, for the interaction of a high-energy photon with such an electron to take place, the photon must scatter and sustain a loss in energy. Such a scatter of a high-energy photon off a free or loosely bound atomic electron is termed *Compton scatter*. Figure 13 depicts the initial and final velocity vectors of the photon and electron in the plane the scatter takes place. For the photon energy range of interest in medicine, Compton scatter essentially involves only outer-atomic-shell electrons, as depicted, because they are more loosely bound. From basic conservation of energy and momentum equations with the parameters shown in Figure 13, and using $E_0 = p_0c$ and $E_f = p_f c$ (photons), we find an expression for the final photon energy in terms of the initial photon energy, the electron rest mass, and the photon scatter angle:

$$E_f = \frac{E_0}{1 + \frac{E_0}{m_e c^2} (1 - \cos \theta)} \quad (34)$$

Figure 14a plots the final photon energy as a function of scatter angle for 140- and 511-keV incident photon energies. As expected, the final photon energy falls off smoothly with increasing angle corresponding to a more energetic recoiling electron. In terms of wave parameters, because photon energy is directly related to its wavelength, the photon undergoes a wavelength shift as a result of Compton scatter.

High-energy photon detectors are sensitive only to the ionization produced by the recoil electrons. The interactions of recoil electrons in matter have been described in the previous section. For loosely bound electrons, the recoil electron energy is given by the difference between the initial and final photon energies, $E_0 - E_f$. For the gamma-ray energies of interest in nuclear medicine, the recoil electron is absorbed within a few millimeters or less, depending on the absorbing medium and electron energy. The recoil electron energy T_{\max} will be maximum when the scattered photon energy is lowest, which is when the photon is backscattered ($\theta = 180^\circ$ in Eq. 34):

$$T_{\max} = E_0 - E_f(\theta=180) = \frac{2E_0^2}{2E_0 + m_e c^2} \quad (35)$$

This equation defines what is known as the Compton edge in gamma-ray spectroscopy. For example, for 140- and 511-keV incident photon energies, the theoretical maximum recoil electron energies for the Compton edge are 50 and 340 keV, respectively. In reality, because of detector energy resolution blurring effects, the measured maximum Compton electron energy will not be sharply defined. For an appreciable range of angles θ near $\theta = 180^\circ$, $\cos(\theta)$ is near -1 and so the final photon energy E_f in Eq. (34) remains close to the value $E_0/[1 + (2E_0/m_e c^2)]$ and the recoil energy distribution forms a peak near T_{\max} in Eq. (35). Note that regardless of scatter angle, the Compton-scattered photon energy never vanishes. A photon cannot transfer all of its energy to an unbound electron in a scatter event.

The Compton scatter photon angular distribution is given by the Klein-Nishina formula for the differential scattering cross section for a photon with an unbound electron (Knoll, 1989):

$$\frac{d\sigma_c}{d\Omega} = r_0^2 \frac{1 + \cos^2 \theta}{2} \frac{1}{[1 + \alpha(1 - \cos \theta)]^2} \left\{ 1 + \frac{\alpha^2 (1 - \cos \theta)^2}{(1 + \cos^2 \theta)[1 + \alpha(1 - \cos \theta)]} \right\} \quad (36)$$

where θ is the polar angle the photon scatters into, r_0 is the classical electron radius, and $\alpha = E_0/m_e c^2$. Because Compton scatter involves free electrons, all materials absorb essentially the same amount of radiation per electron through this process. Because most materials have nearly the same number of electrons per gram, the Compton absorption probability per gram is nearly the same for all materials. Thus, the shapes of the curves in Figure 14 are independent of Z . The total probability of Compton scatter per atom depends on the number of scatter

electron targets available, which increases linearly with Z , the atomic number of the medium. Because we have assumed that all the electrons are essentially free and independent of one another, to obtain the differential cross section per atom we simply multiply Eq. (36) by Z . To obtain the absorption coefficient, τ_c per centimeter, we multiply by N , the atomic number density. That is, the absorption coefficient is proportional to the total number of electrons NZ per unit volume. The first factor in Eq. (36) is essentially the formula for classical *Thomson scatter*, where the electron does not recoil. The next factors take into account the electron recoil and the number of photons scattered into unit solid angle $d\Omega$ at θ is reduced from the classical case by these factors. Figure 14b shows the Compton scatter angle distribution. Small-angle scatter involving low energy and momentum transfer to the atomic electron is most likely, especially for higher incident photon energy.

For lower incident photon energies, the distribution has a trend toward that of the classical Thomson scattering distribution with the characteristic $1 + \cos^2 \theta$ dependence. The classical Thomson scatter phenomenon describes the emission of radiation by a charged particle that has been accelerated by the absorption of incoming electromagnetic radiation. Classically, when electromagnetic radiation encounters a loosely bound electron, the induced acceleration causes the electron to reradiate some of the electromagnetic energy. Because the electron's acceleration will be greatest for a direct hit, emission in the backward direction is favored. For grazing hits, much of the incident electromagnetic energy will be preserved (less will be transferred to the electron) and concentrated in the forward direction. Thus, in the classical case, the flux of radiation is higher in the forward and backward directions, as can be seen in Figure 14b. The Compton effect is the quantum mechanics extension of this classical phenomenon. Thus, for lower incident photon energies, forward and backward

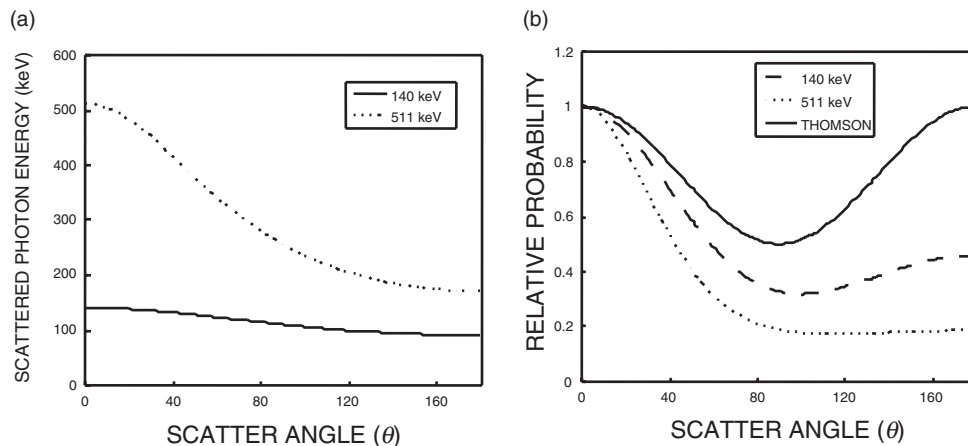


FIGURE 14 (a) Compton scatter photon energy as a function of scatter angle for 140- and 511-keV incident photon energy. (b) Compton scatter probability as a function of scatter angle for 140- and 511-keV incident photon energy and for very low photon energy where the distribution follows the classical Thomson distribution.

Compton scattering is more likely than scattering at 90° , as can be seen by the fall and rise of the scatter probability with increasing angles for the low energy (140-keV) curve. Integration of Eq. (36) over $d\Omega$ gives an expression for the total cross section for a Compton scatter to occur with an individual electron (Heitler, 1960):

$$\sigma_c = 2\pi r_e^2 \left\{ \frac{1+\alpha}{\alpha^2} \left[\frac{2(1+\alpha)}{1+2\alpha} - \frac{1}{\alpha} \ln(1+2\alpha) \right] + \frac{1}{2\alpha} \ln(1+2\alpha) - \frac{1+3\alpha}{(1+2\alpha)^2} \right\} \quad (37)$$

which starts off roughly at 6 barns ($1 \text{ barn} = 10^{-24} \text{ cm}^2$) at 10 keV and strongly decreases with higher energy. Values for the Compton scatter cross section are larger for lower energies. This function for lead and water is depicted in Figure 15. For photon energies greater than 100 keV, $> 99\%$ of all interactions in water are due to Compton scatter. The situation is drastically different in lead. For 140 keV, photoelectric absorption is roughly 10 times more likely than Compton scatter, and, at 511 keV, the two processes are roughly equally likely.

a. Coherent and Incoherent Scatter

If the struck atomic electron is instead strongly bound to and not removed from the atom, Eq. (34) still holds, but the photon momentum and energy is transferred to the entire atom which recoils with the bound electron. Hence the m_e in Eq. (34) should be replaced by the entire mass of the

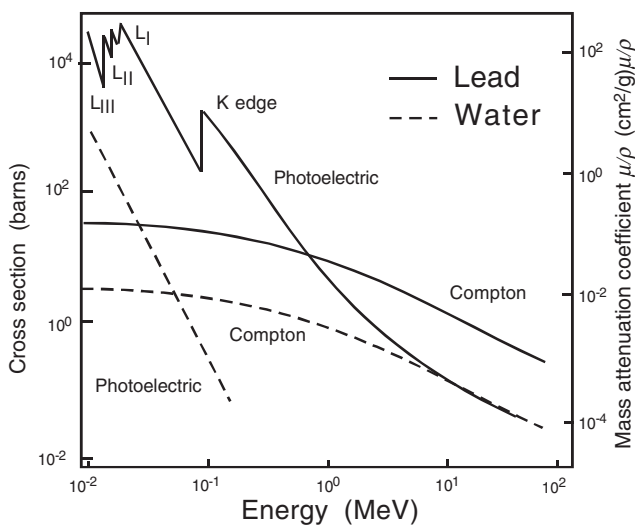


FIGURE 15 Form of Compton scatter and photoelectric absorption cross sections (left axis) and corresponding mass absorption coefficients (right axis) in lead and water as a function of incident photon energy. For gamma-ray energies near the binding energies of K and L shells (88 and 14 keV), the maximum photoelectric absorption occurs when the photon has just enough energy to eject the respective bound electron. (Adapted from Leo, 1987; Knoll, 1989; Heitler, 1960; Siegbahn, 1955.)

atom because the photon scatters off the entire atom. In this case, the scattering is essentially elastic and there is no significant change in photon energy (or wavelength). This type of scattering is termed *Rayleigh scattering*. The scatter probability increases with higher atomic number Z of the scatter medium because a larger fraction of atomic electrons are considered strongly bound. The angular distribution of Rayleigh scattering is unlike that expressed in Eq. (36) because the radiation scattered from all strongly bound atomic electrons interferes coherently. In other words, all the electrons in the atom participate in a coherent manner and the scattering angle is very sharply peaked around $\theta = 0^\circ$. As such, Rayleigh scattering is considered *coherent scattering*. In coherent scattering, the energy of the scattered radiation is essentially the same as the incident energy, the electron is neither excited nor ionized, and the phase of the scattered waves from different electrons are well correlated and only the direction of the photon is changed. To determine the total coherent scatter intensity from the atom, the individual scatter amplitudes from each bound electron are added first and then squared. Compton scatter, on the other hand, is considered *incoherent scattering*. In incoherent scattering, the scattered photon energy is less than the incident value and the difference is transferred to the recoil electron, which either jumps to an excited atomic level or is ejected from the atom. In this case there is no phase relation between the radiation scattered off the individual atomic electrons and the total intensity is obtained by summing the individual electron scatter intensities. The total differential scattering cross section for a photon from an atomic electron is then the sum of the contributions from coherent and incoherent parts. Because coherent scatter is not an effective mechanism for transferring photon energy to matter, it is of little importance in emission imaging.

2. Photoelectric Effect

A gamma ray can transfer all its energy to a bound electron because the atom can absorb some of the recoil momentum, allowing both energy and momentum to be conserved. This process is known as the *photoelectric effect*, the resulting ejected electron is known as a *photoelectron*, and the incident photon disappears. The process is depicted in Figure 16. Because a free electron cannot completely absorb a photon, this effect involves only bound electrons and interactions of this kind mostly take place with electrons in either the inner K shell (as depicted), three L subshells, five M subshells, or seven N subshells. Because a third body, the nucleus, is necessary for conserving momentum, the probability of photoelectric absorption increases rapidly with the strength of the electron binding. That is, the more tightly bound electrons are important for photoelectric absorption. At energies between the binding energies of the K (two-electron) and L (eight-electron)

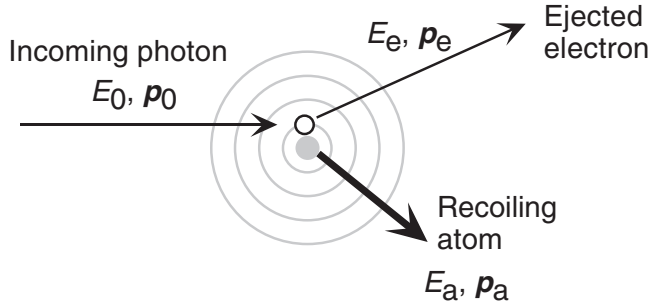


FIGURE 16 Depiction of the photoelectric effect in the plane, which more likely involves an inner-shell electron. Atomic recoil is usually neglected.

shells, the absorption due to outer shells is negligible. For photon energies greater than the binding energy of the K shell, the photoabsorption more likely occurs with a K -shell electron because it is the closest match in energy. In fact, for photon energies above the K shell roughly 80% of all photoelectric absorption involves K -shell electrons (Johns and Cunningham, 1978). For these energies, because the resulting photoelectron is ejected from and no longer bound to the atom, all energies can be absorbed (continuous absorption spectrum). Below the K -shell energy, most of the photoabsorption is due to photons interacting with L and M electrons.

From energy and momentum considerations, the recoil kinetic energy E_a of the atom is of the order $(m_e/M_a)E_e$, where M_a is the atomic mass. Because typically $m_e/M_a \sim 10^{-4}$, we can neglect E_a , and then conservation of energy implies for the kinetic energy of the electron, E_e :

$$E_e = E_0 - E_B \quad (38)$$

where E_B is the binding energy of the atomic electron shell and E_0 is the incident photon energy. The maximum absorption occurs when the photon has just enough energy to eject a bound electron. For incident photon energies greater than the K -shell electron binding energy and less than the rest mass energy of the electron, the cross section for photoelectric emission per atom, σ_p , is given by (Heitler, 1960):

$$\sigma_p = \frac{32}{3} \sqrt{2} \pi r_e^2 \alpha^4 Z^5 \left(\frac{m_e c^2}{E_0} \right)^{7/2} \quad (39)$$

where r_e is again the classical electron radius and α the fine structure constant. For E_0 near the K -, L -, or M -shell binding energy, quantum effects require Eq. (39) to be multiplied by a correction factor that is on the order of and proportional to $(1/Z^2)(m_e c^2/E_0)^{1/2}$, which essentially amplifies the cross section near $E_0 = E_B$ creating a sharp discontinuity called the *absorption edge*. For $E_0 \geq m_e c^2$, relativistic effects modify Eq. (39) with a factor that is proportional to $(m_e c^2/E_0)^{3/2}$. For the K -, L -, M -shell absorption coefficient, τ_K , τ_L , τ_M , we multiply the cross section by the atomic

number density N . Thus, for relevant diagnostic photon energies, the photoabsorption probability varies with atomic number Z somewhere between the third and fifth power, depending on energy, and, away from the absorption edges, the photoabsorption probability varies as $E_0^{-3.5}$. The shape of the photoelectric absorption probability in lead and water as a function of incident photon energy was shown in Figure 15. For diagnostic photon energies, the photoelectric effect is more likely at low energies and Compton scatter is more likely at higher energies. The photoelectric effect is over a factor of 1000 more likely in lead than water for a given energy (Figure 15), even though the ratio of atomic numbers (82 and ~ 7.4) is only slightly over a factor of 10. The ejected electron interacts with matter as described in the Section IVA of this chapter. For photon energies of interest, the ejected photoelectron is absorbed within a few millimeters or less, depending on the absorption material. Because the photoelectric effect creates a vacancy in an inner orbital electron shell, as a result of filling that vacancy, characteristic X-rays or Auger electrons will be emitted.

3. Attenuation of High-Energy Photons

We have seen that gamma rays and annihilation photons are many times more penetrating in matter than are charged particles such as electrons, due to the much smaller cross section of the main interaction processes (Compton scatter and photoelectric absorption for diagnostic photon energies of interest) compared to that of inelastic and elastic beta Coulomb collisions. Unlike charged particles, a beam of photons is not degraded in energy as it passes through matter but, rather, is attenuated in intensity because Compton scatter and the photoelectric effect remove the photon from the beam entirely through either scattering or absorption. Those photons that pass straight through a material are those that have not interacted at all and they therefore retain their full energy. The total number of photons, however, is reduced by the number that have interacted. As for the case of betas, the attenuation of a narrow photon beam in matter follows an exponential form with the penetration depth, except with weaker absorption coefficients:

$$I = I_0 e^{-\mu x} \quad (40)$$

where I_0 is the nonattenuated incident beam intensity, x the absorber thickness, and μ the attenuation coefficient. In contrast to betas, photons do not have a definite maximum range. The quantity I/I_0 can also be viewed as the fraction of photons remaining after the beam has traversed a depth x into the absorber. The μ value is directly related to the total interaction cross section (see Figure 15), which depends on the density and effective atomic number of the absorbing material and the energy of the incoming photons. The total probability of interaction is the sum of the individual Compton scatter (σ_{Compton}) and photoelectric absorption (τ_{Photo}) cross-section contributions:

$$\sigma_T = Z\sigma_{\text{Compton}} + \tau_{\text{Photo}} \quad (41)$$

where, to obtain the total Compton scatter contribution, we have multiplied the interaction cross section by the atomic number Z , representing the number of electrons per atom that may undergo a scatter interaction. Multiplying σ_T by the atomic density N gives us the interaction probability per unit length, or the total linear absorption coefficient, $\mu = N\sigma_T = \sigma_T(N_A\rho/A)$, where N_A is Avogadro's number, ρ the density of the matter, and A the molecular weight. The inverse of μ can be thought of as the mean free path or average distance traveled for the photon between interactions. It turns out that μ increases linearly with ρ . By dividing μ by ρ , these effects are removed. The result is known as the *mass attenuation coefficient* and has units of square centimeters per gram. Tables of μ or μ/ρ for various materials can be found in Siegbahn (1955). For mixtures of elements, the total absorption coefficient follows a form analogous to Eq. (21):

$$\frac{\mu}{\rho} = f_1 \frac{\mu_1}{\rho_1} + f_2 \frac{\mu_2}{\rho_2} + \dots \quad (42)$$

where f_i is the weight fraction of each element making up the mixture.

Figure 17 depicts Monte Carlo-simulated photon interactions in a pixellated array of CsI(Tl) ($Z_{\text{eff}} = 54$, $\rho = 4.51 \text{ g/cm}^3$) crystals from 140-keV photons emanating from a point source located above the array. The exponential behavior of the photon absorption is qualitatively seen in the figure from the higher density of interactions near the top of the array. The corresponding spectrum of absorbed energies is shown at the right of Figure 17. From this spectrum we see the total absorption energy peak at 140 keV, the Cs or I K -shell X-ray escape peak near 105 keV, and a combination of Compton scatter and X-ray interactions at low energies ($\leq 50 \text{ keV}$). A visual comparison with the

Monte Carlo-calculated data for beta interactions shown in Figure 12 demonstrates the discrete versus continuous nature of photon and beta interactions, respectively.

V. EXPLOITING RADIATION INTERACTIONS IN MATTER FOR EMISSION IMAGING

With a basic understanding of how relevant nuclear emissions interact in matter we next turn to how those interactions can be detected and localized in various position-sensitive detectors used in biomedical radioisotope imaging. Parts II–VIII of this book describe in detail imaging detector designs and methodology that have been developed for clinical and research applications. So as not to duplicate this information, in this section we only describe some of the basic preliminary concepts involved in event positioning. A more comprehensive review of available detector technologies can be found in Leo (1987) and Knoll (1989).

All current biomedical radioisotope detection methods use the ionization or excitation created in matter as a result of the partial or full absorption of a nuclear particle's energy. The total amount of energy deposited and recorded in the detector represents the energy of the incoming particle. For charged-particle emission detection, the energy deposition is a direct result of the interaction of the particle's electromagnetic field with atomic electrons of the detection medium and the resultant ionization and excitation are manifested as a track of separated charge or excited electron states centered about the particle's trajectory. For gamma rays, either Compton scatter or photoelectric absorption must first occur, whereby part or all of the energy is transferred to an atomic electron in the absorbing material, which in turn produces the ionization or

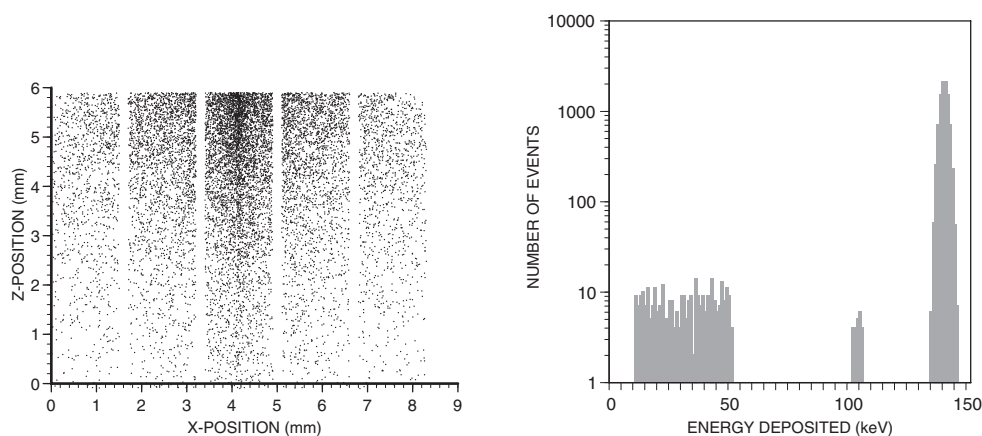


FIGURE 17 Side view of Monte Carlo-simulated interactions produced in a CsI(Tl) crystal array from a point source of 140-keV photons 1 cm above the top of the array. Interactions from 12,000 events are shown. The corresponding calculated spectrum of absorbed interaction energies in the array is shown at the right.

excitation track. In gas-filled detectors (see Bolozdynya *et al.*, Chapter 18 in this book), the deposited energy results in the formation of electron-ion pairs and emission of light photons. For semiconductors (see Wagenaar, Chapter 15 in this volume), the energy deposited is manifested as electron-hole pairs, where an electron from a lattice site is elevated from the valence to the conduction band of the semiconductor leaving a hole behind. We refer to electron-ion or electron-hole pair production as *charged pair* creation. For scintillators (see Wilkinson, Chapter 13 in this volume) the absorbed energy produces either electron-hole pairs if the scintillation material is an inorganic crystal or excitation of molecular valence electrons if it is an organic compound. The ionization and excitation produced with the absorption of a particle in the different types of detectors will create the necessary energy, timing, and positioning information for imaging.

A. Statistics of Ionization Production

For gas-filled and semiconductor detectors the total ionization produced is that which is measured and represents the energy of the incoming particle. An important quantity for a detection medium is the w -value, which is defined as the average energy required to create an electron-ion or electron-hole pair in gases or semiconductors, respectively. In a given ionization medium the w -value is nearly identical for beta or gamma radiation over a large range of energies. This constancy allows a good proportionality between incoming particle energy and amount of ionization produced. Table 1 lists some w -values for common gases and semiconductors along with the ionization potential or band gap. Because much of the absorbed energy is in the form of excitation or other processes that do not result in the liberation of electrons from the parent atomic sites, the w -value for a material is always higher than the binding energy, which is the ionization potential in gases or band gap in semiconductors.

The limit in precision of the energy measurement, or *energy resolution*, depends on the statistical fluctuation of the number N of charged pairs produced. However, if the detector medium completely absorbs the particle's energy, then the standard deviation of N , σ_N is smaller than that

predicted by Poisson statistics ($\sigma_N = \sqrt{N}$) because the creation of each charged pair is correlated with all other charged pairs created. This correlation is a result of the fact that the energy deposited at each interaction and for every event is constrained by the fixed value of the total particle energy absorbed. Thus, in reality $\sigma_N = \sqrt{FN}$, where $F < 1$ is called the *Fano factor* and depends on absorber characteristics. Because of the lower w -values (and therefore larger N) and smaller Fano factors, σ_N/N will be lower and the energy resolution limit higher for semiconductor compared to gaseous detectors.

The factors limiting the energy resolution in scintillation detectors are considerably different. The electronic signals produced by scintillation detectors are a convolution of five factors: (1) the absorption of the particle's energy and excitation/ionization of the scintillator material, (2) light yield from a scintillator due to the deexcitation of molecular energy levels, (3) the collection of that light by the photo-multiplier tube (PMT), (4) the absorption of light photons in and emission of photoelectrons from the photocathode of the PMT, and (5) the collection and amplification of the photoelectron signal in the dynode stages of the PMT. The result is that the fluctuation in the number of electrons measured at the PMT anode is close to that expected from Poisson statistics.

B. Detector and Position-Sensitive Detector Basics

Details of biomedical emission imaging detector designs are given in Parts II–V. Here we briefly describe some basics of signal formation and positioning in gaseous, semiconductor, and scintillation detectors used in medical nuclear emission imaging. In nuclear medicine, it is necessary to image the distribution of photon (gamma ray or annihilation photon) and sometimes beta emissions from the body. For photons, this is achieved by (1) proper *collimation*, which gives a preferred direction to the photons entering the camera for a high spatial correlation between those photons detected and those emitted from the body and (2) proper electronic segmentation of the particular radiation detector used. In the case of gamma-ray imaging, a physical collimator is used to absorb those photons not entering the camera in a particular direction (see Zeng, Chapter 8 in this book). In the case of a coincident annihilation photon imaging system (e.g. a PET camera), the directionality is provided electronically from the coincident detector interactions of the two oppositely directed annihilation photons (see Lewellen, Watson, and Cherry, Chapters 10–12 in this book). In the case of direct beta imaging (see Rogers *et al.*, Chapter 19 in this book), no collimation is necessary. The short range of betas in tissue and detector materials provides a natural collimation mechanism.

In this section, we describe the position-sensitive radiation detector portion of an emission imaging system. An emission *camera* senses the two-dimensional coordinates of the particles of interest emitted from the body through the

TABLE 1 w -Values and Ionization Potential or Band Gap Values for Some Common Gases and Semiconductors

Detector Material	w -Value (eV)	Ionization Potential or Band Gap (eV)
Argon gas	26.3	15.8
Xe gas	21.9	12.1
Si	3.62	1.12
CdTe	4.43	1.47

interactions occurring in the detector. By accumulating and positioning many such events, an image of the projected radioisotope distribution may be formed.

1. Ionization Detection in Gases

a. Ionization Chambers

The traversal of an ionizing particle through a volume of gas creates a track of electron and positive-ion pairs. The quantity of ionization produced can be measured by applying an appropriate electric field across the medium with the use of anode and cathode electrodes configured with the cathode at a negative potential with respect to the anode. This is known as an *ion chamber*. The electric field must be strong enough to overcome the mutual attraction between electrons and ions or else they will recombine. The electrons will drift toward the anode and the positive ions toward the cathode. These motions will induce charge on the respective electrodes and will cause the anode potential to be changed slightly. The voltage induced on the anode by the electron's motion is proportional to the fraction of voltage through which the electron drops before collection, and the same is true for the ion. Because the total voltage drop traversed for the particles is equal to that applied across the system, in principle the total charge induced on the anode is independent of the original position of the ion pair. However, because the positive ion is much more massive than the electron, it moves much slower and the voltage signal induced has a much smaller slope than that for the electron. Thus, there will be a systematic variation in shape of the signal induced with the location and orientation of the ionization track. It is also important that the chamber be free from impurities. The presence of impurities adds to the variation of the signal with drift distance due to trapping of drifting charge. The anode is usually maintained at a virtual ground by means of a very large resistor value R_L connected to a voltage source that allows the induced charge to leak off the chamber capacitance C at a rate controlled by the time constant $R_L C$.

If all the electrons and ions are completely collected, the final voltage signal will be proportional to the total ionization produced and hence the particle energy, independent of the distribution of ionization events in the chamber. In reality, however, because of the typically long ion drift times (~ 1 ms), it would be impractical to wait for complete ion signal collection, and so usually the detector signals are derived from the electron induced component only, which is on the order of 100 to 1000 times faster. This is accomplished by using pulse-shaping circuits with an appropriately short time constant. However, now the proportionality between the ionization produced and induced voltage is lost because the voltage through which the electrons fall prior to collection varies with position. The design of electron signal-only ion chambers aims to

maintain a constant voltage drop for the majority of electron tracks produced from ionizing radiation. Figure 18 shows a ^{207}Bi energy spectrum measured in a small parallel-plate grid ionization chamber (Levin *et al.*, 1993) filled with 60 atm (1.4 g/cm^3) of xenon gas at room temperature. Due to the high energy resolution, the system easily resolves the daughter ^{207}Pb K -shell internal conversion electron lines (at 570 and 976 keV). The system also resolves the full energy peaks (at 570 and 1063 keV) consisting of either the absorbed K -shell electron summed with the detected ^{207}Pb K -shell X-rays or Auger electrons or, with lower probability, the absorbed gamma rays.

One of the most common ion chamber configurations is a cylindrical cathode with a thin anode wire at the axis. Because the voltage at radius r in the chamber, which is essentially a cylindrical capacitor, is $\sim \log(1/r)$, most of the voltage drop for drifting electrons is confined to very near the anode wire independent of where the ionization is created. Because of the relatively low gain in gas ionization chambers, amplifier noise can make a significant contribution to the overall noise and low-noise, charge-sensitive preamplifiers are needed for the charge-voltage conversion and impedance matching to read out the anode signal.

b. Proportional Chambers

A disadvantage of the ion chamber is the relatively small output signal. A high detector gain is desired so that the

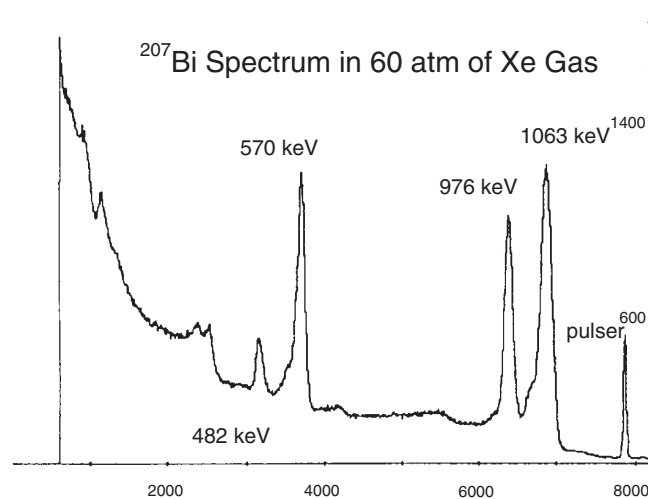


FIGURE 18 ^{207}Bi pulse height spectrum in a 42-cm^3 xenon gas ionization chamber pressurized to 60 atm (1.4 g/cm^3) at room temperature (Levin *et al.*, 1993). The ^{207}Bi source was deposited directly on the cathode within the chamber. The drift electric field was 3.0 kV/cm . The noise subtracted energy resolution of the 976 keV conversion electron peak is 17% full width at half maximum (FWHM). The noise contribution was measured with an electronic pulser.

amplifier noise is not determining the energy resolution and threshold. This can be accomplished by increasing the drift electric field strength. If the drift electric field is increased substantially, the drifting electrons can acquire enough kinetic energy to cause further ionization as a result of molecular collisions. Again, if the electric field is strong enough, this accelerating ionization charge can produce further ionization and so on, with the result of an avalanche of electron and positive ion pairs that can consist of 10^4 – 10^6 times the original ionization charge. If the electric field is not too high, the charge induced on the electrodes is still proportional to the initial ionization charge, which is proportional to the incoming energy deposited. The resulting configuration is called a *proportional chamber*. At too high an electric field, the amount of ionization charge created can actually modify the electric field and lower the gain for each event and the proportionality between input energy and output charge is not preserved. This also can happen if the incoming radiation flux is very high and the ion drift velocity is relatively low to the point that the electric field is altered. These problems of ion accumulation are referred to as *space charge buildup*. Because it is desired that the charge multiplication factor is fairly independent of the origin of ionization creation, this suggests the need for a high electric field gradient.

To attain high fields, usually a thin wire anode and coaxial cylindrical cathode are used as depicted in Figure 19a and most of the multiplication takes place in the intense field region near the anode wire. This implies that of the total electrons created, most undergo a relatively small voltage drop as they drift toward the anode. Because the anode is at a high positive electric potential with respect to the cathode, the positive ions, on the other hand, undergo a much larger voltage drop as they drift toward the cathode. Because the signal induced on the anode from a drifting charge carrier depends on the voltage drop encountered, most of the signal induced on the anode is due to the motion of positive ions away from the anode rather than from electron motion toward the anode and a negative signal is induced on the anode. In addition to ionization produced in the avalanche process, excited gas atoms and molecules that are formed deexcite, giving rise to photons with high enough energy to ionize materials inside the chamber. This problem can be solved by adding a polyatomic gas, such as methane, to act

as a quencher that absorbs the unwanted photons and dissipates their energy into other processes besides ionization.

c. Position-Sensitive (Imaging) Gas Detectors

We have discussed basic configurations used to collect ionization produced in a gas in order to measure an incoming particle's energy. For imaging, the location of the ionization created must also be precisely defined. The basic technique to achieve imaging in gaseous detectors is through *segmentation* of the anode and cathodes. The spatial resolution is thus determined by the particular electrode configurations. The gas-filled detector designs that are being used in biomedical emission imaging (Jeavons *et al.*, 1999; Visvikis *et al.*, 1997) are essentially position-sensitive proportional chambers that are a combination of basic elements of a multiwire proportional chamber (MWPC) and drift chamber (Leo, 1987; Knoll, 1989).

A basic configuration of a MWPC is shown in Figure 19b. Each wire acts as an independent proportional chamber. If the anode wire spacing is a few millimeters and the anode to cathode spacing is just under a centimeter, the electric field lines are essentially constant and perpendicular to the cathode surface, except for the region very close to the anode wires where the field takes on the characteristic $1/r$ dependence of a proportional chamber. Electrons and ions created in the constant field region drift along the field lines toward the nearest anode wire and cathode plane, respectively. As with the basic proportional chamber, most of the induced anode signal is due to the positive ion motion away from the anode. The wire closest to the ionization event records the largest (negative) signal. This basic configuration allows ionization positioning information in one dimension. For information about the second coordinate, a second parallel plane of anode wires that are oriented perpendicular to the first is integrated into the same chamber. The cathode planes may also be formed as sets of segmented strips in alternating orthogonal orientations, as for the anode (Leo, 1987; Knoll, 1989). An alternate to the planar design of a MWPC shown in Figure 19b may be formed by configuring a set of parallel closely packed cylindrical proportional cells that each look similar to that depicted in Figure 19a, except instead of the cathode surface being a solid shell it is composed of wires (Leo, 1987; Knoll, 1989). Adjacent cells then share cathode wires.

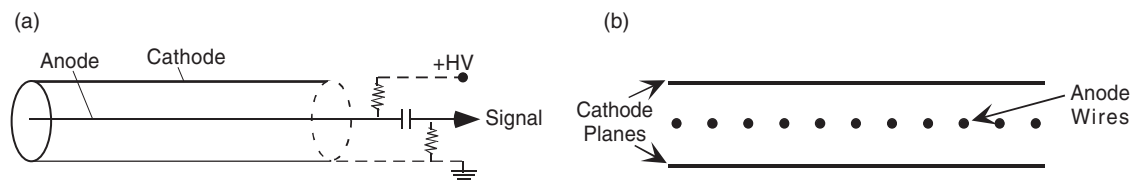


FIGURE 19 (a) Schematic drawing of a basic gas proportional ionization cell. (b) Basic multiwire proportional chamber (MWPC) configuration. In the multiwire position-sensitive MWPC, typically a negative voltage is applied to the cathode.

There are three basic readout methods for obtaining positioning information in MWPCs. They all exploit the fact that the avalanche at the anode is highly localized along the length of the wires. The *center of gravity* method uses cathode strip signals. Because the induced signals are the largest on the closest strip to the avalanche, the avalanche point in any one direction is obtained by calculating the center of gravity of the induced signals. The *charge division* method uses the fact that the anode wire is resistive and the signal measured on either end of the wire depends on how far from the respective end the avalanche appears. The *delay line* technique measures the time difference between the arrival of the signals at the ends of a delay line that is coupled to the cathode or anode for a measure of the avalanche location along the respective electrode segment. Spatial and temporal resolution in these systems are determined by the anode wire spacing. Spatial resolution is on the order of one-half the wire spacing. The temporal resolution is related to the time it takes for electrons to drift one-half the wire spacing, which for 2-mm spacing and typical drift velocities of 5 cm/ μ s is about 20 ns.

The efficiency and sensitivity of MWPCs depend on factors such as the activity strength, dE/dx in the gas, the gas density, the presence of impurities, the anode cathode spacing, the applied high voltage, the gating and electronic threshold for noise rejection, and other factors that affect the total charge created and collected. Typically, flux rates no higher than 10^3 – 10^4 counts per second per mm of wire can be measured. The MWPCs may be stacked together at various orientations to provide x - y position information for a variety of beta and high energy photon ionization imagers.

In a drift chamber (Leo, 1987; Knoll, 1989), spatial information is obtained by measuring the electron drift time in an ionization event. If a trigger is available to determine a time reference point for the event and the electron drift velocity is known, the distance from the anode readout wire to the ionization origin may be precisely determined. If the electric field is constant, the drift velocity is constant and there is a linear relationship between drift time and

distance to the anode. A drift cell comprises a cathode at high voltage, the drift region, and an anode, similar in principle to a basic proportional counter. However, for a constant electric field over a relatively large region, a series of field-shaping wires surround the drift region. For the trigger, typically detection of internal scintillation light created from the fill gas itself or an added scintillator is implemented. A typical drift distance is several centimeters. Cells are typically stacked next to or on top of one another to cover a large area (Leo, 1987; Knoll, 1989).

For radioisotope imaging there are many possible configurations of MWPCs and drift detectors and associated readout methods. Hybrid detectors referred to as *gas proportional scintillation counters* combine properties of the proportional counter and scintillation detector. More information on various MWPC designs can be found in Leo (1987), Knoll (1989), and references therein. Some gaseous and hybrid detector designs currently used in emission tomography and beta autoradiography are described in Jeavons *et al.* (1999), Visvikis *et al.* (1997), and Bolozdynya *et al.* (Chapter 18 in this book).

2. Electron-Hole Pair Detection in Semiconductors

The basic operating principle of semiconductor detectors is analogous to that in gas ionization chambers except that a semiconductor crystal instead of a gas fills the space between the anode and cathode. When ionizing radiation is absorbed in the crystal, electron-hole pairs are created rather than electron-ion pairs. The object is again to collect both positive and negative charge carriers on electrodes through the application of an electric field. A semiconductor crystal has a quantized electron energy *band structure* that describes the allowed electron energy states in the crystal lattice (see Figure 20). In a pure crystal, the electron can only lie in the many close-lying electron energy levels of the valence or conduction band and not in the well-defined energy gap E_g between the two energy bands. The interaction of a nuclear particle raises electrons from the valence band, where the electrons are bound to a particular

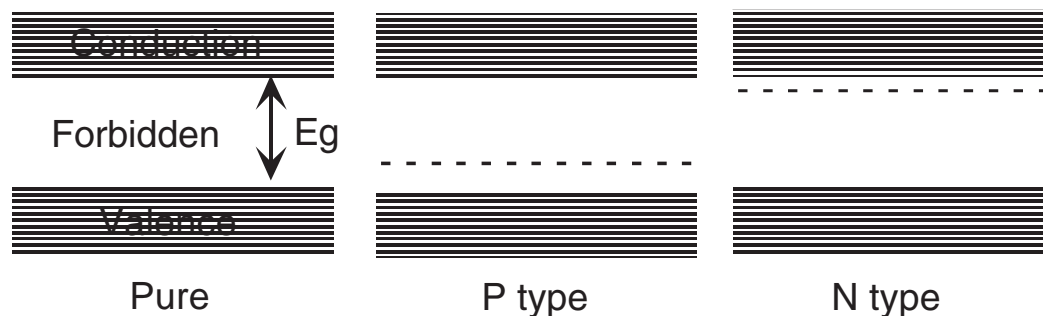


FIGURE 20 Depiction of electron energy band structure for a pure semiconductor crystal and for that with acceptor (P-type) and donor (N-type) impurities. The dotted lines represent impurity energy levels in the forbidden gap of the pure crystal.

lattice site, across the energy gap to the conduction band where the electron is free to move about the crystal lattice. This action leaves a positive *hole* or absence of a valence electron. Under an appropriate electric field the conduction electron will move toward the anode and the positive hole will essentially move toward the cathode through an effective field-induced hopping of valence electrons between neighboring atoms. As for gases, a small energy gap will yield a large number of electron-hole pairs from a particle interaction. Typically only a planar geometry is used for any given single semiconductor device. As is the case for gas detectors, the goal is the complete collection of the electrons and holes created from an ionizing event so that the amplitude of the electrode signals induced is proportional to the number of electrons and holes created.

Not all semiconductors make good detectors. Because of the higher atomic density in semiconductors, trapping of charge carriers at defects or impurities is a bigger problem for most semiconductors than for gases. The extent of these traps determines the lifetimes of the charge carriers. The mobilities of the electron and hole should be high and the lifetimes long for fast signal rise time and efficient charge collection. The conductivity produces a significant leakage current across the cell that could swamp any ionization-produced charge carrier signal. So the purity of semiconductor detector materials must be extraordinarily high (< 1 part in 10^8 impurity level). The main advantage of a semiconductor crystal as an ionization medium is that the w -value is roughly 10 times smaller (see Table 1) and, thus, 10 times more ionization is created than for gases for a given particle energy, which in principle can lead to better energy resolution. Also, semiconductors typically have a higher effective Z and density and, thus, a higher stopping power than for gases. The most common semiconductor crystals that are found in current nuclear medicine cameras are Si and CdZnTe. Properties of some of these materials and a more detailed discussion of semiconductor detector configurations and principles of operation are given in Wagenaar and Levin (Chapters 15 and 16 in this book), and can also be found in Leo (1987) and Knoll (1989).

In reality a semiconductor always contains impurity centers in the crystal lattice and electrons can occupy energy states of an impurity site that fall within the forbidden band of the pure crystal (see Figure 20a). Impurities having energy levels that are initially vacant just above the top of the valence band are termed *acceptors* and are referred to as *P type*. These atoms have an outer electronic structure with one electron less than the host material. A vacant impurity level may be easily filled by thermal excitation of a valence electron from a nearby atom, leaving a hole in that atom. If the number of such holes exceeds that available from the intrinsic thermal excitation of valence electrons, the conductivity will increase. Those impurities that introduce energy

levels that are initially filled just below the conduction band are *donor* or *N type* impurities and are produced by impurities with an outer electronic structure with one more electron than the host material. In that case, an electron occupying such an impurity level may be more easily thermally excited into the conduction band compared to a valence electron, and the conductivity would therefore increase. Because hopping of neighboring host atom valence electrons is energetically unfavorable, the impurity holes left behind are not free to move about and the only contribution to conduction by holes is through intrinsic thermal excitation of valence electrons.

Usually semiconductors contain both acceptor and donor impurities and their effects on conductivity will cancel out. If a material tends to have more acceptors than donors, or vice versa, it is possible to compensate for the increase of conductivity by the addition of an appropriate amount of an impurity so that the material becomes closer to the less conductive intrinsic material. For low leakage current, the conductivity should be low and so the material should be well compensated. Figure 21 shows ^{99m}Tc energy spectra taken in a $3.3\text{-mm}^2 \times 500\text{-}\mu\text{m}$ -thick HgI_2 pixel at room temperature and cooled (Patt *et al.*, 1996). The cooled spectrum has better energy resolution due to lower dark current. The low energy tail on the 140-keV peak is due to incomplete hole collection and incomplete energy deposition in the small detector. Note this high resolution detector resolves some of the *K*-shell *X*-ray lines (in Hg, I, and Pb) and *X*-ray escape peaks associated with ^{99m}Tc transitions and subsequent detection in HgI_2 .

a. Position-Sensitive (Imaging) Semiconductor Detectors

As was the case for gaseous detectors, position sensitivity with semiconductor detectors is obtained from the localization of the charge created from a particle interaction. Position sensitivity in semiconductors can be established by segmenting or pixellating the anode or cathode electrodes. For radioisotope imaging the segmentation is typically sets of square pixels or parallel rectangular strips. The electron-hole pairs created travel along the established electric field lines and induce a signal on the closest electrode(s). In the square-pixel anode readout, the position is determined by that pixel location. In a cross-strip readout, the anode and cathodes are two orthogonal strips of electrodes, and the x - y position is determined by the two individual orthogonal strips that register the largest signal. Unlike in gases, it is difficult to configure many electrode planes within the same monolithic crystal, and usually only one plane of cathode and anode pixels is configured in any given device. Because the typical gain of semiconductor devices is relatively low, low-noise charge-sensitive preamplifier electronics are required for charge-to-voltage conversion and impedance matching for each semiconductor electronic channel. Various configurations of planar electrode patterns used in medical

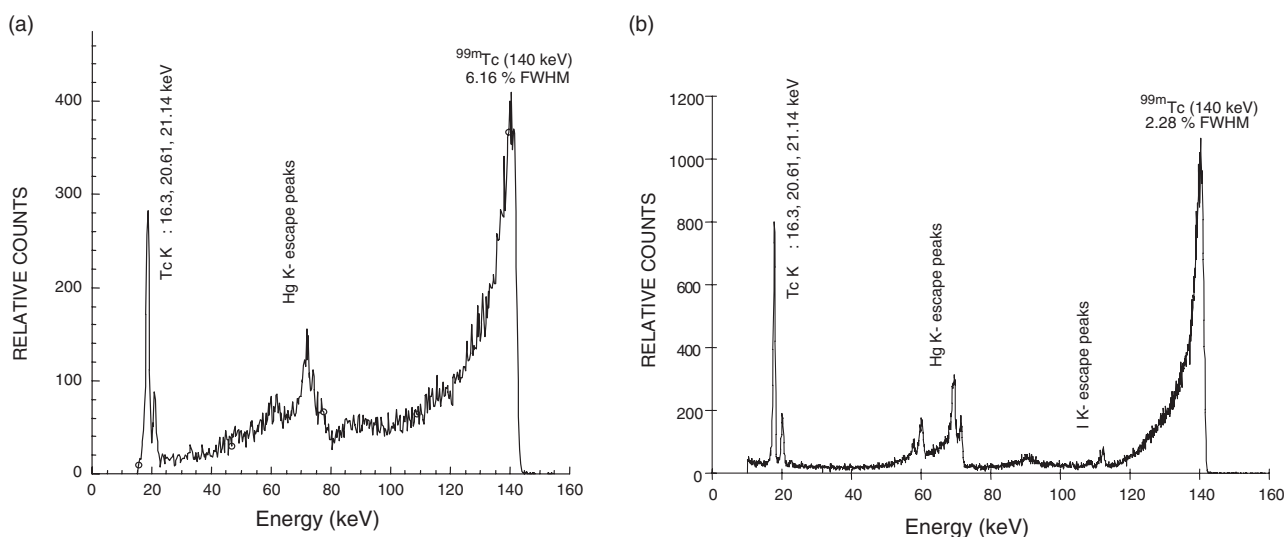


FIGURE 21 ^{99m}Tc spectra measured in a 3-mm² HgI₂ detector (a) at room temperature and (b) cooled to 0°C. (From Patt *et al.*, 1996.)

imaging are described in more detail in Wagenaar and Levin (Chapters 15 and 16 in this book).

3. Light Detection in Scintillators

Scintillation detectors are currently the most commonly used technology in nuclear medicine. Most often inorganic scintillators are used because they have highest stopping power for gamma rays and annihilation photons, are relatively fast and bright, have emission spectra that are well matched to the absorption spectra of PMTs, and are relatively inexpensive to manufacture. For direct beta imaging, organic plastic scintillators can be used. PMTs are fast and generate gains $> 10^5$ with very little noise. The principles of PMT operation are described in detail in (Chapters 13 and 14 in this book). Alternative semiconductor photodetector designs such as the photodiode (PD), avalanche photodiode (APD), and drift photodiode (DPD) are discussed in Pichler and Levin (Chapters 14 and 16 in this book). Because of the high charge amplification ($\geq 10^5$ at ~ 1 kV bias), and low capacitance associated with the PMT, front-end amplifier noise is not important in limiting the signal-to-noise ratio (SNR) and energy threshold. A basic current-to-voltage converter and line driver used to match impedance for input into the next amplification stage are required for a PMT. However, because of the relatively low gain and high noise contribution of a semiconductor photodetector, amplifier noise can make a significant contribution. Thus, for each semiconductor photodetector channel used, special low-noise, charge-sensitive preamplifiers are needed for the charge-voltage conversion and impedance matching (see Chapters 14 and 16 in this book). Figure 22 shows a collimated ^{57}Co source spectrum measured in a NaI(Tl)-PMT scintillation detector. The 136.5-keV ^{57}Co line is

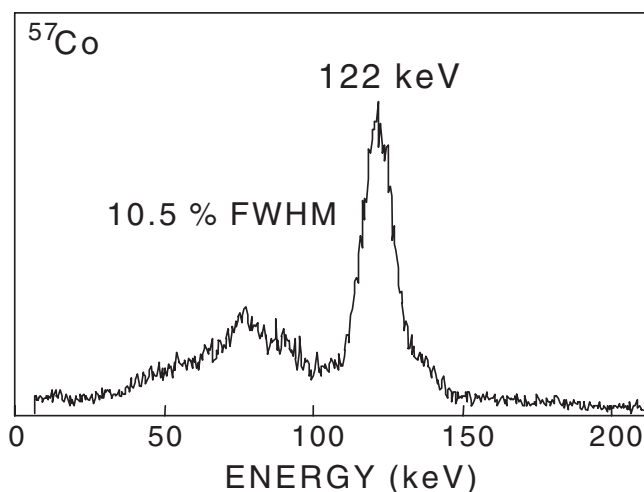


FIGURE 22 ^{57}Co (122-keV) gamma-ray spectrum in a $6 \times 6 \times 0.6$ cm³ NaI(Tl) crystal coupled to a PMT.

the cause of the bump on the high energy portion of the 122-keV peak. The hump centered at around 75 keV is due to the absorption of Pb K-shell X-rays (~ 72 keV) and the backscattered photon peak at 90 keV ($140 - 50 = 90$ keV; see Eq. 34).

a. Mechanism of Light Production in Inorganic Scintillation Crystals

For completeness we give a brief description of the inorganic crystal scintillation mechanism. More detail can be found in Wilkinson (Chapter 13 in this book) and in Leo (1987), Knoll (1989), and Birks (1964). As for semiconductor crystals (see Figure 20), inorganic scintillation crystals have

an electronic band structure that dictates the allowed electron energy states in the lattice. A particle interaction in a pure inorganic crystal results in the liberation of electrons from the valence band into the conduction band. After some time, the conduction electrons will recombine with holes with the resulting excitation energy E_g converted into light. However, this process is inefficient and the wavelength of light corresponding to E_g is below the visible range, which is not useful for a standard PMT. The luminescent efficiency is improved and the wavelength of emission increased into the visible range by the addition of a small amount of a suitable activator impurity, which effectively produces electron energy levels in the previously forbidden gap between the valence and conduction bands. The excitation energy in the host material is then transferred to the energy levels of the impurity centers in the crystal lattice, which deexcite with the emission of longer wavelength photons that overlap with the visible range. Properties of various scintillators are given in Wilkinson (Chapter 13 in this book).

b. Position-Sensitive (Imaging) Scintillation Detectors

The most common camera currently found in radioisotope imaging is based on position-sensitive scintillation detectors. Position-sensitive scintillation detectors localize the light flash created within the crystal. This may be achieved by segmenting the crystal, the photodetector, or both. Figure 23 depicts three basic configurations of two-dimensional position-sensing scintillation detectors known as *gamma-ray cameras*. In this figure we also show a gamma-ray collimator (see Gunter, Chapter 8 in this book), which absorbs photons not entering the camera in a preferred direction. The position-sensitive scintillation detector used in coincident annihilation photon imaging does not require such a physical collimator, but the light-pulse positioning concepts are similar.

The position-sensitive scintillation light detector consists of a scintillation crystal(s) and a position-sensitive photodetector. The scintillation crystal may be a single-crystal slab or a set of small discrete or pseudodiscrete crystals. For the single crystal design (Fig. 23a) the scintillation light diffuses and reflects throughout the crystal and the light pulse is positioned by an appropriate weighted mean of the individual photodetector signals over their respective positions.

This weighted-mean position calculation is also used with the multiplexed discrete crystal design (Fig. 23b), which comprises an array of optically isolated crystals coupled through a light diffuser to photodetectors. In this crystal design, the light created is confined to one crystal and collected onto a smaller area on the photodetector plane compared to that shown in Figure 23a. With a weighted-mean calculation, the detector intrinsic spatial resolution in this design will be finer than the photodetector anode readout pitch and on the order of the crystal pixel size. Because more crystals can be decoded than there are photodetectors, this is an efficient technique for reducing the number of electronic processing channels required. A variation on this theme is used in the PET block detector (Casey and Nutt, 1986), where pseudo-discrete crystals (partially optically coupled) are used and the light is diffused within the scintillation crystal itself and the PMT entrance window rather than in a separate light diffuser. In the completely discrete system (Fig. 23c), the imaging array is formed by many small, optically isolated crystals, each coupled one to one with a separate photodetector channel. All light created in one crystal is focused onto one photodetector. As for the multiplexed discrete crystal design, the detector spatial resolution is determined by the crystal width. The position-sensitive photodetector array (depicted at the bottom of each configuration in Figure 23) might be an array of individual PMTs, position sensitive PMT(s) with segmented electrodes,

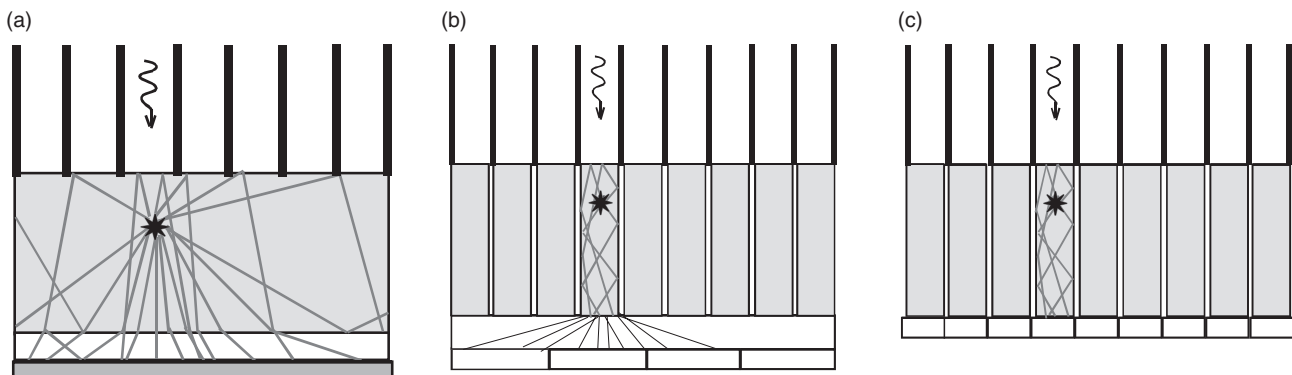


FIGURE 23 Possible coupling schemes of crystals to photodetector arrays in scintillation cameras. (a) Light sharing over the position-sensitive photodetector is natural in single-crystal slab design, but a light diffuser may be needed for optimal light spread. (b) Light multiplexing is necessary when there are fewer readout channels than individual crystals. A light diffuser might be required in this situation as well. (c) No light multiplexing is necessary when the crystals are coupled one to one with the photodetector pixels. Light created in a crystal is focused onto one photodetector element. Photodetector shown at bottom of each drawing may be either an array of individual PMTs, a multianode PMT, or a semiconductor photodetector array. Only fraction of the detector field of view (FOV) and a parallel-hole collimator design are shown.

or a semiconductor photodetector array. Because of its high light yield, appropriate emission spectrum, and reasonable cost, NaI(Tl) is the crystal of choice for commercial systems. Because of its relatively low cost compared to arrays, a single continuous crystal is typically used in clinical systems. Because of its high gain, low noise, and reasonable cost the PMT is currently the photodetector of choice in nuclear medicine.

VI. PHYSICAL FACTORS THAT DETERMINE THE FUNDAMENTAL SPATIAL RESOLUTION LIMIT IN NUCLEAR EMISSION IMAGING

A. Overview of Physical Factors That Affect Emission Imaging Performance

There are many physical factors that effect radioisotope imaging performance. Many of these topics are discussed in detail in later chapters of this book. In planar gamma ray imaging and single-photon emission computed tomography (SPECT) (see Zeng, Gunter, Genna, and Levin, Chapters 7, 8, 9, and 16 in this book), the sensitivity and typically spatial resolution are limited by the properties of the physical collimator used. In certain cases, the spatial resolution is strongly affected by the intrinsic spatial resolution and object scatter as well. For a source deep within tissue, photon attenuation can significantly reduce available counts and cause nonuniform image artifacts. King (Chapter 22 in this book) discusses approaches to attenuation correction in SPECT. Image contrast between different activity structures is affected by the incorrectly positioned Compton scatter photons. The largest positioning errors originate from scatter that occurs from within the imaging subject. Because Compton scatter photons are less energetic than the initial photon, Compton scatter effects can be reduced by accepting only those events that have total energy within a small range (window) around the photopeak energy. To achieve this scatter reduction while still maintaining high sensitivity, the energy resolution of the system should be high; hence, the scintillation crystal should be bright and the electronic noise low. King (Chapter 22 in this book) discusses other scatter rejection methods for SPECT. Having high crystal photofraction will contribute to improved sensitivity by ensuring that a high fraction of detected events fall in the photopeak.

In coincident annihilation photon imaging systems such as PET (see Lewellen, Watson, and Cherry, Chapters 10–12 in this book), because no physical collimator is used, the system sensitivity is determined by the system intrinsic and geometric efficiencies for 511-keV annihilation photons. For good efficiency the detector material should have high Z and density for good photon-stopping power and cover as large an area as possible around the imaging subject. As is the

case for single-photon imaging, annihilation photon attenuation within the body can significantly reduce available counts and produce nonuniform image artifacts. This problem is actually worse for coincident annihilation photon imaging because there are two detected photons per event, and hence there is a higher probability for an interaction to occur. Attenuation correction techniques for PET are discussed in Lewellen (Chapter 10 in this book). The spatial resolution is determined by the fluctuations of positron range and annihilation photon noncollinearity, and intrinsic detector resolution. Image contrast is affected by Compton scatter, random or accidental coincidences, and detector dead time. Compton scatter positioning errors are more prominent in annihilation photon imaging due to the broader scatter distribution and reduced (for 2D acquisition) or absence of (in 3D acquisition) physical collimation (see Lewellen, Watson, and Cherry, Chapters 10–12 in this book). Compton scatter can be somewhat reduced by energy windowing, but again, to maintain high sensitivity (fewer rejected events), the energy resolution and photofraction should be high so that a narrow photopeak window will contain a high fraction of the incoming events. Other scatter rejection techniques for PET are discussed in Lewellen, Watson, and Cherry (Chapters 10–12 in this book).

Random coincidences in annihilation photon imaging are background events in which two different nuclei each contribute one detected annihilation photon within the coincidence resolving time of the system. The effect of random coincidences on image contrast can be reduced by having excellent coincident time resolution and by reducing the detected activity. High coincident resolving time requires a fast, bright scintillation crystal or detector and low electronic noise. Standard techniques for random-coincidence reduction are discussed in Lewellen, Watson, and Cherry (Chapters 10–12 in this book). Detector dead time due to pulse pile-up degrades energy and spatial resolutions, resulting in reduced PET image contrast at high count rates. Random-coincidence and dead-time effects can be reduced if fast detectors are implemented. Standard dead-time correction for PET systems is discussed in Lewellen, Watson, and Cherry (Chapters 10–12 in this book).

B. What Is the Fundamental Spatial Resolution Limit in Radioisotope Imaging?

The importance of rodent (mouse and rat) models for human disease has spawned an interest in high spatial resolution medical imaging. To be able to resolve fine structures, high spatial sampling of the signal from the object is required. There has especially been a recent interest in the development of high spatial resolution radioisotope imaging systems for small animals (see Cherry and Levin, Chapters 12 and 16 in this book and the references therein) due to the inherent functional biological information that may be obtained. These

developments motivate the question: What is the fundamental spatial resolution that can be achieved with radioisotope imaging? It is well known that other radiology imaging modalities such as X-ray computed tomography (CT) or magnetic resonance imaging (MRI) can achieve submillimeter spatial resolution. This allows tiny structures of the animal subject to be resolved with those systems. Could this submillimeter spatial resolution be possible for nuclear medicine techniques such as SPECT and PET? If so, would the sensitivity per resolution element be adequate enough to fully use this spatial resolution potential? These physical questions are addressed in this section.

1. Spatial Resolution Potential for Single-Photon Emission Imaging Systems

In most gamma-ray imaging systems, the achievable spatial resolution is limited by the collimator properties. The well-known collimator equations for spatial resolution and sensitivity in parallel-hole, converging, diverging, and pinhole collimators are presented in (Chapter 8, Gunter in this book). The collimator spatial resolution is quite variable. For the parallel-hole design, the spatial resolution depends on the hole size, height, linear attenuation coefficient at the photon energy of interest, and distance of the radioisotope source from the collimator. For the pinhole design, in addition to similar parameters, the resolution also depends on the apex angle of the pinhole cone. The total system spatial resolution is a convolution of the collimator and intrinsic detector resolutions. We assume here that these contributions are approximately Gaussian in shape and we ignore scatter effects on the full width at half maximum (FWHM) spatial resolution.

Figure 24 plots the system point source spatial resolution for different source–collimator distances as a function of intrinsic detector spatial resolution for parallel-hole and

pinhole collimators at 140 keV. In these calculations, we have assumed a hole diameter of 1.2 mm, a collimator height of 4.0 cm, $\mu = 27\text{cm}^{-1}$ for lead at 140 keV, a septal thickness of 0.2 mm for the parallel-hole design, and for the pinhole an apex angle of 45° and source locations along its axis. The results will change for different values of these parameters, but the assumed parameters promote high spatial resolution performance and will serve as a basis to understand spatial resolution limitations. For the pinhole calculations we have included the magnification factor x/h , where x is the source–aperture distance and h the height of the collimator. The magnifying property of pinhole collimators can provide an improvement in overall system spatial resolution in the image plane when the source–aperture distance is less than the collimator height because the resulting image magnification factor reduces the effective contribution of the intrinsic detector resolution.

Higher intrinsic detector resolutions can be achieved by segmenting the detector into tiny pixels. In this way, the intrinsic spatial resolution is selected to be on the order of the detector pixel size (see Chapter 16 in this book). For fine sampling of the radioisotope distribution, these pixels must be closely spaced with little dead area in between pixels.

Figure 24 shows the well-known feature that in single-photon imaging the spatial resolution improves with decreasing source–collimator distance and hole diameter. For source–collimator distances less than 1 cm (i.e., shallow structures), the spatial resolution achievable is essentially determined by the hole diameter (1.2 mm for Figure 24) and the intrinsic detector resolution. To achieve submillimeter spatial resolution with collimated gamma-ray imaging, we could decrease the hole diameter d into the submillimeter range, be extremely close to the object, and use a finely pixellated detector design. However, because the geometric efficiency is on the order of d^2 for both the parallel- and

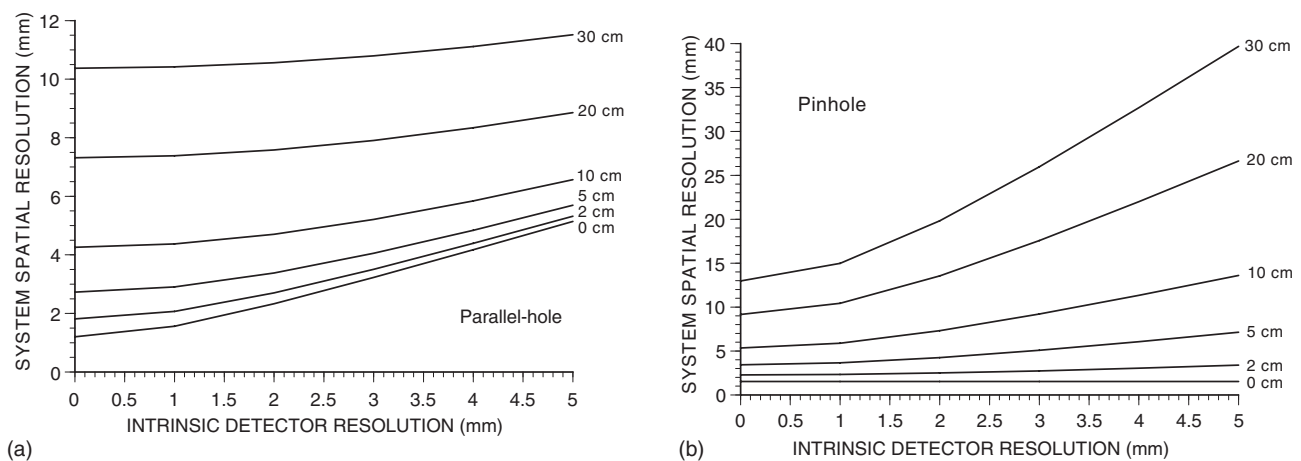


FIGURE 24 Calculated spatial resolution (FWHM) as a function of intrinsic detector spatial resolution for various source–collimator distances for (a) parallel-hole and (b) pinhole collimators at 140 keV. We have assumed a collimator hole diameter of 1.2 mm, height of 4.0 cm, and $\mu = 27\text{cm}^{-1}$ for lead at 140 keV; and for the pinhole an apex angle of 45° and the magnification factor have been included.

pinhole collimators (see Chapter 8 in this book, for efficiency equations), the system sensitivity would also significantly drop. For example, with our parameters ($d = 1.2$ mm) and $x = 2$ cm, the system spatial resolutions at 140 keV are 2.1 and 2.3 mm with corresponding geometric efficiencies of 5×10^{-5} and 2×10^{-4} , respectively, for the parallel- and pinhole collimators using 1-mm intrinsic spatial resolution. This gives sensitivities of 2.0 and 7.3 cps/ μ Ci, respectively, for the parallel- and pinhole designs for a 140-keV point source in air and a single planar detector array. With one-half the hole diameter (600 μ m), the system spatial resolutions at 2.0 cm would be 1.3 and 1.4 mm, respectively, for the parallel- and pinhole designs, but the collimator efficiency values would drop to 1×10^{-5} and 6×10^{-5} , respectively. This yields low sensitivity values of 0.4 and 2.2 cps/ μ Ci, respectively, for the two designs for 140-keV photons.

For planar imaging, because the standard deviation per image pixel is \sqrt{N} , where N is the number of events in that pixel, the image pixel SNR is \sqrt{N} . If the system resolution drops by a factor of two, the number of events must increase by a factor of four to maintain the same average SNR per image pixel. In tomographic (SPECT) imaging, the pixel values are highly correlated. It turns out that if the resolution cell size decreases by two, the required number of events for constant uncertainty must increase by roughly a factor of eight (Budinger *et al.*, 1978). So, the significantly reduced sensitivity values for the 600- μ m-hole collimators may not allow these systems to attain their resolution potential of approximately 1 mm due to poor SNR per image pixel.

The sensitivity in a parallel-hole collimator system does not change significantly with source-to-collimator distance. However, the pinhole sensitivity drops off as $1/x^2$, where x is source-aperture distance. Thus, moving the detector closer to the source allows us to regain sensitivity in a pinhole design. Another basic solution to improving the overall system sensitivity while maintaining high resolution is to increase the number of pinhole or parallel-hole detector arrays and surround the object so that more area surrounding the radioisotope distribution is covered. Such a small-diameter ring system consisting of multiple, finely spaced, pinhole-collimated, pixellated detector arrays is under development (Pang *et al.*, 1994).

Note that the resolution values plotted in Figure 24 are for 140-keV photons. Significantly improved spatial resolution may also be achieved by using lower energy sources (e.g., ^{125}I) with a submillimeter pinhole collimator. However, due to the high degree of attenuation for such low-energy photons, such a system would be limited to imaging very shallow structures within tissue.

2. Spatial Resolution Potential for Coincident Annihilation Photon Imaging Systems

The main advantages of annihilation photon imaging systems are the improved sensitivity and spatial resolution

potential because no physical collimator is required. The direction of annihilation photon emission is defined electronically by the line connecting the two interactions on opposing detectors. However, both oppositely directed photons must be detected, so the extent of the sensitivity improvement depends on the geometric and intrinsic efficiency of the detector gantry. Although there is no collimator resolution component in annihilation photon imaging, there are two additional effects that contribute to spatial resolution blurring: positron range and annihilation photon noncollinearity.

In radioisotope emission imaging, we are after the exact location of the emitter nucleus. Unlike in single-photon emission imaging, photons from positron annihilation do not originate from the same location as the particle that was emitted. There is a fluctuation in penetration or range of the energetic positron in tissue due to the varying positron emission energy and direction and attenuating properties of the tissue (see Figures 5 and 10). More energetic particles penetrate deeper. There is a fluctuation in the end point of the positron's track and therefore in the origin of the annihilation photons. Thus, the precision in localizing a positron emitter is compromised by the positron's range. For best spatial resolution, the positron emitter chosen should have the smallest maximum decay energy. Attempts to measure (Derenzo, 1979; Phelps *et al.*, 1975) and calculate (Levin and Hoffman, 1999; Palmer and Brownell, 1992) the effect of positron range on resolution have been made. A histogram of calculated positron annihilation end-point coordinates along any given direction is cusplike, as shown in Figure 25 for ^{18}F positrons. These calculated data result from Monte Carlo simulations of electron trajectories from a point source that includes effects of the positron energy spectrum, multiple Coulomb elastic scattering from the nucleus, hard elastic collisions with electrons, and energy loss due to ionization and excitation (see Section IVA). The cusplike shape is due to the fact that many of the positrons are emitted with low (< 50 keV) energy and thus will be absorbed very close to the location of emission. This cusplike structure can be approximated by a sum of two decaying exponential functions, one with a fast decay constant (short ranges) and the other with a slow decay constant (large ranges) (see Derenzo *et al.*, 1979 and Levin *et al.*, 1999):

$$F(x) = Ce^{-k_1x} + (1-C)e^{-k_2x} \quad x \geq 0 \quad (42)$$

The best fit parameters to this equation for the simulated cusplike positron range functions for ^{18}F , ^{11}C , ^{13}N , and ^{15}O are given in Table 2. Because ^{18}F positron emission has a relatively low maximum and mean kinetic energy of 635 and 250 keV, respectively, the calculated maximum range is only ~ 2 mm with a FWHM in one dimension on the order of 0.1 mm. For positron emitters with higher maximum positron emission energy, the blurring due to positron range

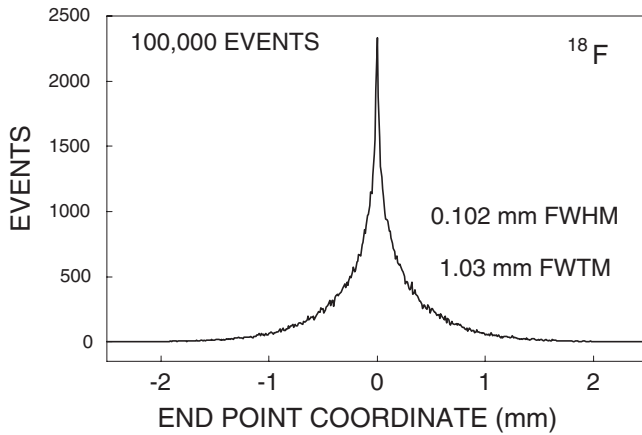


FIGURE 25 A histogram of x -coordinates of positron annihilation endpoints from a Monte Carlo simulation of ^{18}F positron trajectories in water for a point source (see Figure 10). FWHM, full width at half maximum; FWTM, full width at tenth maximum. (Adapted from Levin and Hoffman, 1999.)

TABLE 2 Best-Fit Parameters of Equation (42) to the Simulated 1D Cusplike Positron Range Distributions in Water for Four Common Positron Emitters.^a

	^{18}F	^{11}C	^{13}N	^{15}O
C	0.52	0.49	0.43	0.38
$k_1(\text{mm}^{-1})$	37.9	23.8	20.2	18.1
$k_2(\text{mm}^{-1})$	3.10	1.81	1.42	0.90

^a See Fig. 25; $x \geq 0$ and normalized for y -intercept of 1.

TABLE 3 Calculated Range-Blurring Contributions for Common Positron Emitters^a

Isotope	Average Positron Kinetic Energy (keV)	Maximum Positron Kinetic Energy (keV)	FWHM (mm)	FWTM (mm)
^{18}F	250	635	0.10	1.03
^{11}C	390	970	0.19	1.86
^{13}N	490	1190	0.28	2.53
^{15}O	740	1720	0.50	4.14

^a From [16].

will be greater. Table 3 gives the FWHM and full width at tenth maximum (FWTM) of Monte Carlo simulation-calculated positron range cusp functions for four of the most commonly used positron emitters (Levin and Hoffman, 1999). It should be noted that for a cusplike function, FWHM and FWTM do not have a well-defined meaning. Note the positron range blurring contribution depends only on the isotope and material traversed and is independent of system parameters.

Positioning algorithms in annihilation photon coincidence imaging assume that annihilation photons are emitted in completely opposite directions (180° apart). In reality if the positron-electron system is not at rest at annihilation, the two annihilation photons cannot be completely collinear as a result of momentum conservation. It turns out from detailed experiments that the positron annihilation photon angular deviation from collinearity is small and the angular distribution is approximately Gaussian-shaped with 0.25° or 0.0044 radian FWHM for a point source (Levin and Hoffman, 1999). The extent of resolution blurring from annihilation photon noncollinearity depends on the system detector spacing (system diameter in the case of dedicated-ring PET) because the further the detection points are from the annihilation origin, the larger the positioning error introduced by the assumption of photon collinearity. Using the formula for arc length, we multiply the system radius by the angular deviation to determine the linear deviation introduced. The linear deviation (FWHM) is roughly 0.0022 and D , where D is the system diameter in millimeters, independent of the isotope used. For a 20- and 80-cm detector separation, for example, the deviation at FWHM introduced is roughly 0.4 and 1.8 mm, respectively. Thus, for optimal spatial resolution, the system detector separation, (or diameter) should be small. Note that as the detector separation is decreased, the sensitivity significantly increases in coincidence photon imaging.

The last important contribution to the annihilation photon system spatial resolution is due to the intrinsic detector resolution, which is also an important factor in close proximity single-photon imaging. For annihilation photon coincidence imaging, however, a measurement of point-source response (i.e., *point spread function*) is triangular in shape with FWHM on the order of one-half the detector element size, assuming source-to-detector distances much greater than the detector element size. Thus, for example, the intrinsic detector resolution contributes on the order of 2 mm when the crystal pixel width is 4 mm. For better spatial resolution, finer detector elements should be used. The system spatial resolution will always be greater than the detector half width contribution due to positron range and noncollinearity contributions. Other blurring effects in annihilation photon imaging such as off-axis detector penetration, detector Compton scatter, and inadequate sampling of the signal for image reconstruction can be compensated for with proper detector design and are covered in Lewellen and Cherry, Chapters 10 and 12 in this book.

Thus, the fundamental spatial resolution in annihilation photon coincidence imaging is determined by positron range, photon noncollinearity and detector pixel size. The total system resolution is a mathematical convolution of the three distributions. Figure 26 plots the distributions (blurring functions) for these three physical factors as well as the total system spatial resolution function for an ^{18}F point source in a 20-cm-diameter animal system and an 80-cm-diameter

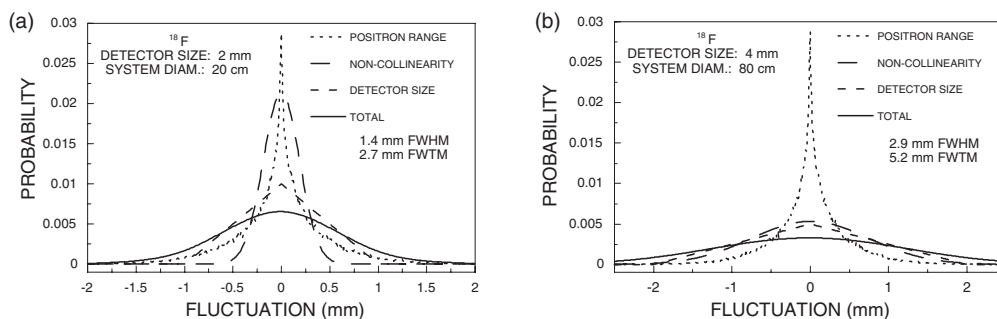


FIGURE 26 Spatial resolution blurring functions for positron range, photon noncollinearity, and detector size using an ^{18}F point source for (a) 20-cm- and (b) 80-cm-diameter systems. (Adapted from Levin and Hoffman, 1999.)

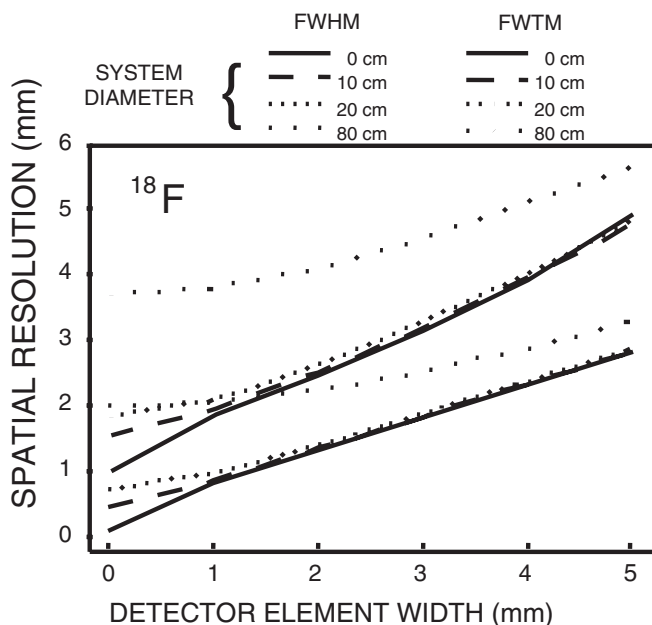


FIGURE 27 Calculated ^{18}F PET system spatial resolution (FWHM and FWTM) as a function of detector element width for various system diameters. For 1-mm detectors, 20-cm detector separation, the spatial resolution potential is ~ 750 mm FWHM for coincident annihilation photon imaging.

human system. Figure 27 plots the ^{18}F system resolution (FWHM and FWTM) as a function of detector element size for various system diameters. Figure 27 may be useful for the design of high spatial resolution ^{18}F coincidence imaging systems. Resolution limit curves for other common PET isotopes are given in Levin and Hoffman (1999).

Figure 26 shows that for small system diameters, the system spatial resolution for ^{18}F is limited by the detector element width and for large diameters by the noncollinearity effect. From Figure 27, we see that it is only possible to push the spatial resolution of PET into the micron range by using a low-energy position emitter such as ^{18}F and ≤ 1 -mm detector pixels. For a 10-cm-diameter PET system with 1-mm-wide detectors, the resolution limit would be

roughly 750 μm , which is certainly comparable to or better than most CT or MRI system spatial resolutions. Further improvements in spatial resolution for ^{18}F imaging would be possible by using highly pixellated, submicron semiconductor detector arrays with adequate stopping power for 511-keV photons. The SNR varies as the inverse cube root of the detector sampling distance (Sorenson and Phelps, 1987). So, by decreasing the intrinsic detector resolution by a factor of two, the sensitivity drops by roughly a factor of eight. The sensitivity of a PET system consisting of a ring of detectors for a point source at its center is roughly $2\pi RH/4\pi R^2 \sim 1/R$, where R is the system radius and H is the axial extent of the ring. Thus, submillimeter spatial resolution may be realized with adequate image SNR by moving the detectors as close as possible to the imaged object.

References

- Bethe, H. (1953). Moliere's theory of multiple scattering. *Phys. Rev.* **89**, 1256–1266.
- Birks, J. B. (1964). *Theory and Practice of Scintillation Counting*. Pergamon, Oxford.
- Budinger, T. F., Greenberg, W. L., Derenzo, S. E., *et al.* (1978). Quantitative potentials of dynamic emission computed tomography. *J. Nucl. Med.* **19**, 309.
- Casey, M. E., and Nutt, R. (1986). A Multicrystal Two Dimensional BGO Detector System for Positron Emission Tomography. *IEEE Trans. Nucl. Sci.* **33**(1), 460–463.
- Chadwick, J. (1914). The intensity distribution in magnetic spectrum of b-rays of radium B & C. *Verhandl. Deut. Physik. Ges.* **16**, 383.
- Daniel, H. (1968). Shapes of beta-ray spectra. *Rev. Mod. Phys.* **40**, 659–672.
- Derenzo, S. E. (1979). Precision measurement of annihilation point spread distributions for medically important positron emitters. In 'Positron Annihilation'. (R. R. Hasiguti, and K. Fujiwara, eds.), pp. 819–823, Japan Institute of Metals, Sendai, Japan.
- Evans, R. D. (1972). "The Atomic Nucleus." McGraw-Hill, New York.
- Heitler, W. (1960). "The Quantum Theory of Radiation." 3rd ed. Oxford University Press.
- Jevons, A. P., Chandler, R. A., and Dettmar, C. A. R. (1999). A 3D HIDAC-PET Camera with Sub-millimetre Resolution for Imaging Small Animals. *IEEE Trans. Nucl. Sci.* **46**(3), 468–473.
- Johns, H. E., and Cunningham, J. R. (1978). 3rd Ed. *The Physics of Radiology*. C Thomas, Springfield.

- Knoll, G. F. (1989). "Radiation Detection and Measurement," 2nd ed. Wiley, New York.
- Lederer, C. M., Hollander, J. M., and Perlman, I. (1967). "Table of Isotopes," 6th ed. Wiley, New York.
- Leo, W. R. (1987). "Techniques for Nuclear and Particle Physics." Springer-Verlag, Berlin.
- Levin, C. S., Germani, J., Markey, J. (1993). Charge collection and energy resolution studies in compressed xenon gas near its critical point. *Nucl. Instr. Meth. Phys. Res. A* **332**, 206–214.
- Levin, C. S., and Hoffman, E. J. (1999). Calculation of positron range and its effect on the fundamental limit of positron emission tomography system spatial resolution. *Phys. Med. Biol.* **44**, 781–799.
- Levin, C. S., MacDonald, L. R., Tornai, M. P., and Hoffman, E. J. (1996). Optimizing light collection from thin scintillators used in a beta-ray camera for surgical use. *IEEE Tran. Nucl. Sci.* **43**, 2053–2060.
- Meyerhof, W. E. (1967). "Elements of Nuclear Physics." McGraw-Hill, New York.
- Palmer, M. R., and Brownell, G. L. (1992). Annihilation density distribution calculations for medically important positron emitters. *IEEE Trans. Med. Imaging* **11**, 373–378.
- Pang, I., Barrett, H. H., Chen, J-C *et al.* (1994). Physical evaluation of a four-dimensional brain imager. [Abstract]. *J. Nucl. Med.* **35**(5), 28P.
- Patt, B. E., Iwaczyk, J. S., Wang, Y. J., *et al.* (1996). Mercuric Iodide Photodetector Arrays for Gamma-Ray Imaging. *Nucl. Inst. & Meth. A* **380**, 295–300.
- Pauli, W. (1934). "Rapports du 7^e Conseil de Physique Solvay, Brussels, 1933." Gauthier-Villars, Paris.
- Phelps, M. E., Hoffman E. J., and Huang, S. (1975). Effects of positron range on spatial resolution. *J. Nucl. Med.* **16**, 649–652.
- Ritson, D. M. (1961). *Techniques of High Energy Physics*. Interscience, New York.
- Roll, F. David (ed.) (1977). "Nuclear Medicine Physics, Instrumentation and Agents." CV Mosby, Saint Louis.
- Siegban, K. (ed.) (1955). *Beta and Gamma Ray Spectroscopy*. Interscience, New York.
- Sorenson, J. A., and Phelps, M. E. (1987). "Physics in Nuclear Medicine," 2nd ed. W. B. Saunders, Philadelphia.
- Visvikis, D., Ott, R. J., Wells, K., and Flower, M. A. *et al.* (1997). Performance characterisation of large area BaF₂-TMAE detectors for use in a whole body clinical PET camera. *Nucl. Instr. Meth. Phys. Res. A* **392**, 414–420.
- Wu, C. S., and Moskowski, S. A. (1966). "Beta Decay." Interscience, New York.